Upwelling Circulation on the Oregon Continental Shelf. Part II: Simulations and Comparisons with Observations

J. FEDERIUK AND J. S. ALLEN

College of Oceanic and Atmospheric Sciences, Oregon State University, Corvallis, Oregon

(Manuscript received 21 December 1993, in final form 2 November 1994)

ABSTRACT

Sixty-day simulations of flow on the Oregon continental shelf are performed using the Blumberg and Mellor sigma coordinate, primitive equation model. The model is two-dimensional (an across-shelf section) with high spatial resolution and realistic shelf topography. Forcing consists of surface heat flux, either hourly or low-pass filtered wind stress, and in one case, a constant alongshore pressure gradient. Model results are compared with current and hydrographic measurements from the CUE-2 program. The horizontal scale of the alongshore coastal jet is significantly influenced by the structure of the initial density and velocity fields. The model successfully reproduces the vertical shear in the alongshore velocity field v, but the model's mean v field is too strongly southward, and the variance in both the u and v fields is underpredicted. Inclusion of the alongshore pressure gradient, while improving prediction of the mean alongshore velocities, does not improve the model–data correlation. The time-mean model density agrees with observations at middepths over the shelf, but shows larger values than observed near the surface. The results demonstrate the importance of including a surface heat flux and of specifying realistic initial density and alongshore velocity fields.

1. Introduction

The Blumberg and Mellor (1987) primitive equation model, with its use of sigma coordinates and embedded turbulence closure scheme, is widely used to study a variety of problems in estuarine and coastal flows. This and other numerical models are clearly of value for process studies where geometry and forcing are idealized. However, success in using numerical models for simulations of real continental shelf flow fields has been rather limited. In an effort to overcome two particular limitations of previous modeling efforts, the lack of sufficient resolution and overly simplified turbulent mixing parameterizations, we apply a high-resolution, two-dimensional version of the Blumberg and Mellor model to flow over the Oregon continental shelf, using realistic shelf topography and wind forcing from the 1973 Coastal Upwelling Experiment (CUE-2), and initializing with the observed density field. In Allen et al. (1995), hereafter referred to as Part 1, the model's response to idealized forcing is examined. In this study, the model is forced with the observed hourly wind stress and surface heat flux and in one case with an additional constant alongshore pressure gradient. The results are compared with measured current and density fields. Additional experiments are performed to investigate the model's response to different specifications of the wind forcing, including a low-pass filtered version of the wind stress, wind stress calculated from measurements at a nearby shore station, and wind stress that varies across the shelf. Although the shelf flow field off the Oregon coast is known to be three-dimensional so that direct model–data comparisons have limited applicability, two-dimensional studies are clearly important prerequisites for more complicated three-dimensional applications.

A general understanding of the summer upwelling circulation on the Oregon shelf has emerged from the CUE-2 study and from subsequent measurements. The CUE-2 program involved hydrographic and current measurements and included a line of current meter moorings and CTD surveys at 45°15′N during July and August of 1973 (e.g., see Smith 1981; Huyer 1976). Along the Oregon coast the upwelling season usually occurs from April through September. Upwelling favorable alongshore winds with velocities of up to 8 m s^{-1} occur intermittently throughout the season on timescales of 3–7 days, causing discrete upwelling and relaxation events. The upwelling flow field is characterized by a southward coastal jet structure in the alongshore current, extending across most of the approximately 25-km wide shelf. Stratification is quite high ($\Delta\sigma_\theta \approx 2$ kg m^{-3} over the top 200 m), due in part to the Columbia River plume, and the coastal jet is surface intensified. The strong stratification allows the formation of surface fronts related to upwelling and relaxation cycles. A poleward undercurrent is often seen over the upper slope and outer shelf but may be weak

Corresponding author address: Prof. J. S. Allen, College of Oceanic and Atmospheric Sciences, Oregon State University, Oceanography Admin. Bldg. 104, Corvallis, OR 97331-5503.

or nonexistent during strong upwelling events (Smith 1981).

In spite of the intensive analysis of the CUE-2 data (e.g., see references in Smith 1981; Huyer 1983) many questions remain unresolved about the nature of the flow, particularly about the across-shelf circulation, the turbulent mixing and stability of the flow in the surface and bottom boundary layers and in the upwelling front, and the three-dimensional characteristics of the circulation. Some of these questions can be addressed by numerical modeling, although so far, models with adequate resolution have been limited to two-dimensional geometries. This study goes beyond previous modeling efforts of the Pacific Northwest shelf in the use of realistic shelf bottom topography, high spatial resolution, and inclusion of a turbulence closure submodel.

Hickey and Hamilton (1980) applied the two-dimensional nonlinear model of Hamilton and Rattray (1978) to time-dependent flow over the Oregon shelf. They compared results from a rather coarse-resolution model (4 km horizontally and 12.5 m vertically) to CTD and current meter measurements from the WISP experiment during February and March of 1975. It was found that the model had limited capability for reproducing the observed density field for periods of more than a few days, and grossly underpredicted the energy in the alongshore flow. The coarse vertical resolution precluded an evaluation of the role of vertical mixing. Using a linearized version of the same two-dimensional model in a subsequent study of seasonal timescale variability, Werner and Hickey (1983) found that imposing a constant alongshore pressure gradient improved prediction of the undercurrent that is present in time-averaged observations. In another study of time-averaged flow, Mellor (1986) used a two-dimensional version of the Blumberg and Mellor (1987) model to study the climatological mean features of California coastal waters. He also prescribed an alongshore pressure gradient, applied as a sea surface elevation gradient plus a density gradient, and found that with the alongshore pressure gradient, the model produced a poleward undercurrent.

In a two-dimensional modeling study, Chen and Wang (1990) performed a 103-day simulation of flow on the Northern California shelf during the 1982 Coastal Ocean Dynamics Experiment (CODE 2). They used a nonlinear finite-difference primitive equation model with a level-2 Mellor–Yamada turbulence closure scheme, a rectangular Cartesian coordinate grid with horizontal resolution of 2 km, and a vertical resolution that was 2.5 m in the surface boundary layer and varied from 5 to 180 m below the boundary layer. The model was able to reproduce the observed density field and the alongshore velocity fluctuations remarkably well, but the model's alongshore velocity was too high and the observed undercurrent was not produced. The model also had limited success predicting across-shelf flow below the mixed layer. They speculated that inclusion of an alongshore pressure gradient might improve the fit to the data by slowing the southward alongshore jet and balancing an across-shelf return flow in the interior. A recent study by Zamudio and López (1994) extended a version of the Chen and Wang (1990) model to include alongshore pressure fluctuations calculated from a linear coastally trapped wave model. They found that including the alongshore pressure gradient produced slightly higher correlations between model and observed alongshore velocities, but at the cost of reducing the already underpredicted standard deviations of both u and v velocities. Correlations between the model and observed u velocities were not substantially affected by including the alongshore pressure gradient.

A time-dependent alongshore pressure gradient undoubtedly plays a role in the coastal dynamics of the Pacific Northwest, as illustrated by estimates of observed momentum balances (Allen and Smith 1981; Hickey 1984) and by the success of coastally trapped wave models (Halliwell and Allen 1984; Battisti and Hickey 1984) in predicting the time variation of coastal sea level and alongshore currents. We test whether inclusion of a simple, time-invariant pressure gradient can improve the simulation of event-scale dynamics in a two-dimensional model.

We pursue here a study of the circulation over the Oregon continental shelf by application of the Blumberg–Mellor (1987) model to two-dimensional simulations of upwelling flows during CUE-2. We believe that two-dimensional model simulations and direct model–data comparisons are useful to assess modeling capabilities and are necessary precursors to three-dimensional simulations. The organization of this paper is as follows. The model initialization and forcing is described in section 2. Results of the experiments are presented in section 3. In section 4, model results are compared with observations from the CUE-2 experiment. A discussion and summary are given in section 5.

2. Model initialization and forcing

The model equations and boundary conditions are described in Part 1, sections 2 and 3. The horizontal across-shelf coordinate is x with (u, v) the horizontal across-shelf and alongshore velocity components, respectively. The vertical coordinate is σ, and ω is a velocity component normal to σ surfaces. The domain (Fig. 1) is 100 km wide with a maximum depth of 500 m and is bounded offshore by a rigid wall. Horizontal grid spacing is 0.5 km. In the vertical, uniform grid spacing in σ with 60 grid intervals is used, so that the vertical resolution varies from 0.17 m at the coast to 8.33 m where the water depth is 500 m. Potential density σ_θ is used as in Part 1 in place of temperature and salinity.

Model experiments cover the 60-day period, 29 June–28 August 1973, of the CUE-2 measurement

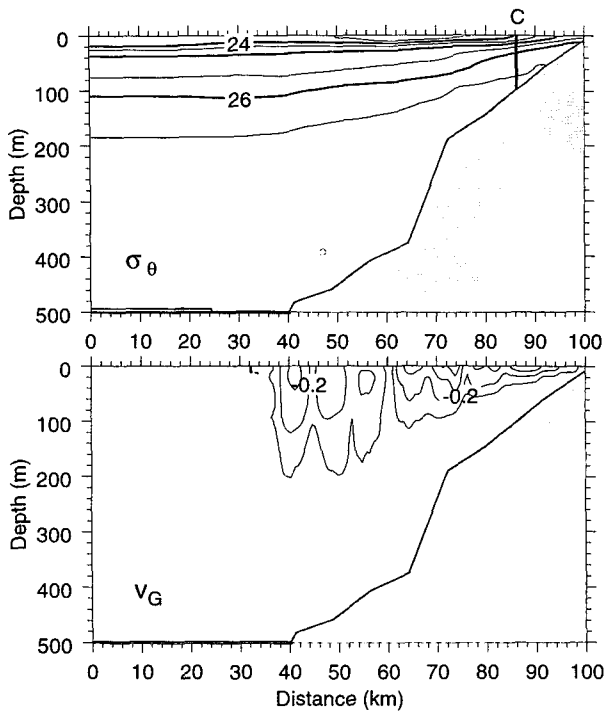

FIG. 1. The model domain and the density σ_θ and associated geostrophic alongshore velocity v_G used for initializing model runs. The contour intervals are $\Delta\sigma_\theta = 0.5$ kg m^{-3} and $\Delta v_G = 0.1$ m s^{-1}. The location of the Carnation and buoy B moorings at the 100-m isobath is indicated by C.

program. Hydrographic CTD surveys (Huyer and Gilbert 1974) of an across-shelf section at 45°15'N provide data for initialization of the model and for comparison with model output on days 15 and 55 of the experiments. Potential density is computed from the CTD temperature and salinity measurements using the standard UNESCO (1983) formulas. Data from the CTD surveys, which extended to 85 km offshore with typical station spacing of 8 km over the shelf (4 km inshore of about 20 km), are gridded using objective mapping with correlation scales of 11 km horizontally and 10 m vertically. Measurements from the farthest offshore station (85 km offshore) are extrapolated unchanged out to 100 km. The horizontal average of the potential density from the 29 June survey is used in Part 1 to initialize the basic-case experiment and is used here to initialize an additional experiment that is started from rest.

The alongshore velocity component v is initialized by computing geostrophic velocities from the initial density field, using 500 m as a level of no motion and extrapolating to shallower water using the method of Reid and Mantyla (1976). Across-shelf velocity u is initialized to zero. Initial potential density σ_θ and alongshore velocity v fields are shown in Fig. 1. Also indicated in Fig. 1 is the location of the Carnation and adjacent buoy B moorings at the 100-m isobath. Velocity measurements at depths of 20.2, 40.4, 60.6, 80.8, and 95.9 m from the Carnation mooring (Pillsbury et al. 1974) and at depths of 3.4, 9.9, and 16.3 m from buoy B (Halpern et al. 1974) are used for comparison with the model output. Winds were measured at buoy B and at Newport (Pittock et al. 1982), located on the coast about 50 km south of the model section. Solar radiation was also measured at buoy B (Reed and Halpern 1974).

The model is forced with north and east components of hourly wind stress, calculated from wind measurements by the method of Large and Pond (1981). In all but one experiment, wind stress calculated from winds measured at buoy B is used. Buoy B wind speed is adjusted to 10-m height using a factor of 1.17, as in Halpern (1976a). Since the model simulation period begins six days before the buoy B measurements, Newport wind stress is used for the first six days. Correlation of buoy B and Newport alongshore wind stress is 0.90 and the means and standard deviations over the common period, 5 July–28 August, are -0.47 ± 0.83 dyn cm^{-2} and -0.28 ± 0.55 dyn cm^{-2}, respectively. For the initial six days the winds are weak, so the Newport wind stress is used without adjustment for the difference in variance. No coordinate rotation is used due to the north–south coastal orientation. The wind field is taken to be spatially uniform, except for one experiment in which a wind stress curl is approximated by linearly interpolating the wind stress from buoy B values 13 km offshore to Newport values at the coast, and using buoy B wind stress offshore of 13 km.

For the experiments where heat flux is included, a uniform diurnal cycle with daily average of 166 W m^{-2} is applied. This value is an estimate (Lentz 1992) of the seasonally averaged net heat flux based on measurements at buoy B during the CUE-2 experiment. The actual measurements do not cover the entire 60-day period of the model runs, so we construct a typical daily cycle with a range of 524 W m^{-2}. Strictly speaking, only the solar insolation component of the net heat flux has a diurnal cycle, but the sensible, latent and longwave radiation components are relatively small. The heat flux is applied as described in Part 1 [Eqs. (2.1d), (2.6d), and (2.10)] with a net flux of $Q_0 = 166$ W m^{-2} and an extinction depth $\lambda_2 = 7.87$ m. This Jerlov (1976) type III depth attenuation is appropriate for relatively turbid coastal waters.

To estimate the additional buoyancy supplied by the Columbia River plume, we idealize the summer plume as approximately 30 km wide and 10 m deep, with a north–south gradient of 0.01 psu km^{-1} (based on figures in Huyer 1977, 1983 and Huyer 1994, personal communication). Mean surface velocity is about 0.4 m s^{-1} southward. Assuming further that the effect of this buoyancy flux is distributed evenly over the 100-km wide domain, the equivalent daily average surface heat flux is 134 W m^{-2}, roughly comparable to the solar heating. Accordingly, in one experiment the net surface heat flux is doubled.

TABLE 1. CUE-2 model experiments. The potential density field from the CUE-2 CTD survey of 29 June 1973 is denoted by σ_{IC}. The corresponding geostrophic velocity is denoted by v_{IC}. For the wind stress components $\tau^{(x)}$ and $\tau^{(y)}$, B indicates measurements at buoy B.

Experiment	Q_0 (W m^{-2})	P_y/ρ_0 (m s^{-2})	$\tau^{(x)}$, $\tau^{(y)}$	Initial conditions
Q	166	0	B hourly	σ_{IC}, v_{IC}
NQ	0	0	B hourly	σ_{IC}, v_{IC}
$Q + P_y$	166	-3.9×10^{-7}	B hourly	σ_{IC}, v_{IC}
Q_{ifi}	166	0	B hourly	horiz. avg. σ_{IC}, $v = 0$
$2Q$	332	0	B hourly	σ_{IC}, v_{IC}
$Q_{\tau_{lp}}$	166	0	B low-passed	σ_{IC}, v_{IC}
Q_{τ_N}	166	0	Newport hourly	σ_{IC}, v_{IC}
$Q_{\nabla\times\tau}$	166	0	B-Newport hourly	σ_{IC}, v_{IC}

The two-dimensional formulation of the model allows consistent specification of an alongshore pressure gradient that is independent of the across-shelf and depth spatial coordinates. Although previous studies have suggested that an alongshore pressure gradient may be important in the seasonal dynamics, it is not obvious that the simplified formulation allowed in the two-dimensional approximation will improve the simulation of variability on shorter than seasonal timescales. To examine the effects of such a pressure gradient, we include a constant alongshore pressure gradient in one experiment, choosing the magnitude so that an interior across-shelf flow distributed uniformly over scale depth H_{SD} would balance the Ekman transport due to the mean wind stress. The mean alongshore wind stress over the 60-day experimental period is $\bar{\tau}^{(y)} = -0.40$ dyn cm^{-2}. With an assumed scale depth $H_{SD} = 100$ m, we obtain $p_y/\rho_0 = \bar{\tau}^{(y)}/(\rho_0 H_{SD}) = -3.90 \times 10^{-7}$ m s^{-2}.

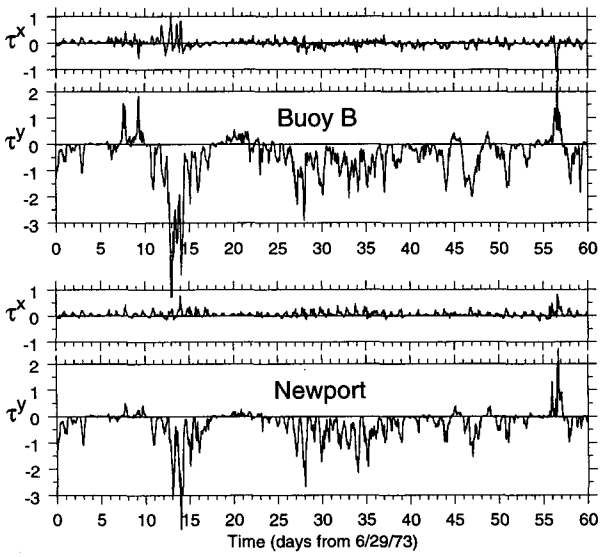

FIG. 2. Hourly wind stress at buoy B and at Newport for the duration of the 60-day runs. Across-shelf components ($\tau^{(x)}$) are positive eastward (onshore) and alongshelf components ($\tau^{(y)}$) are positive northward.

3. Numerical experiments

We concentrate on the results from three main experiments, all initialized with the observed density and corresponding geostrophic alongshore velocity, and all forced with the buoy B hourly wind stress. The basic-case experiment, referred to as the Q experiment, has a surface heat flux applied (a uniform diurnal cycle with daily average of 166 W m^{-2}). No heat flux is imposed in the NQ experiment. Experiment $Q + P_y$ is forced with the same heat flux as Q plus a constant alongshore pressure gradient. In addition, the effects of different initial conditions are examined in an experiment Q_{ifi} that is started from a state of rest with horizontally uniform stratification. Experiment $2Q$ has twice the surface heat flux of Q to simulate the additional buoyancy forcing provided by the Columbia River plume. Results of three other experiments illustrate the effects of varying the wind forcing. Experiment $Q_{\tau_{lp}}$ is forced with buoy B low-pass filtered wind stress, experiment Q_{τ_N} uses Newport hourly wind stress, and experiment $Q_{\nabla\times\tau}$ uses wind stress that varies across-shelf from buoy B values offshore of 13 km to Newport values at the coast. The experiments are summarized in Table 1. Except where noted, model output is averaged over an inertial period and hourly time series are low-pass filtered using a Cosine-Lanczos filter (Denbo et al. 1984), which has a half power point of 46.6 hours.

The hourly wind stress components at buoy B and Newport over the 60-day period, 29 June–28 August, are shown in Fig. 2. There were two strong upwelling (negative $\tau^{(y)}$) events, a 5-day event from days 12–17 (11–16 July), and a period of lighter but more sustained upwelling winds from days 27–38 (26 July–5 August). Between these events winds were generally weaker and variable in direction.

a. Model response from the Q experiment

The model response over the continental shelf for the Q experiment is shown in Fig. 3 for days 15, 25, and 35, which represent both strong upwelling episodes and the interim period of light winds. On day 15, following the first strong upwelling event, isopycnals are upwelled near the coast and the southward jet present

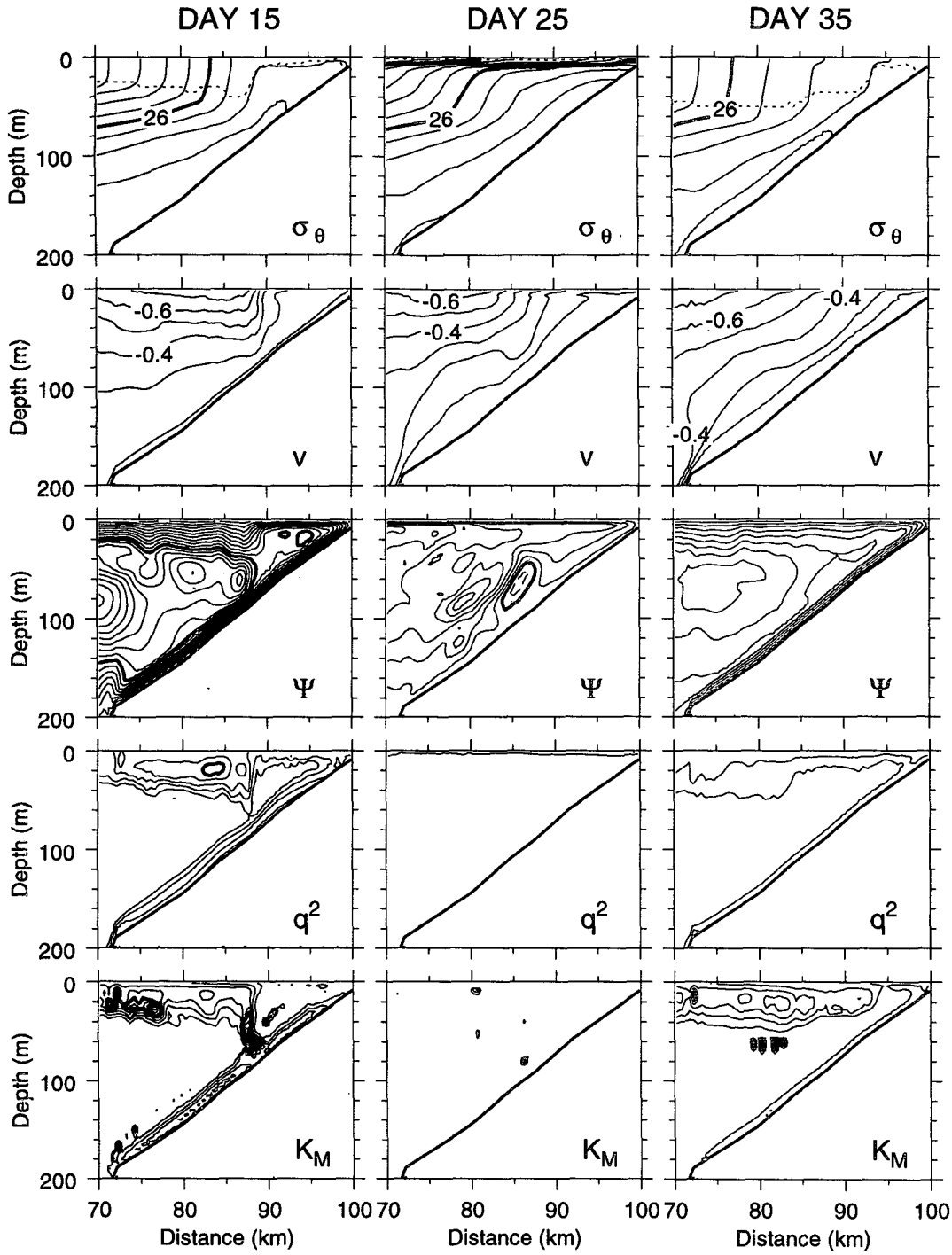

FIG. 3. Fields of the density σ_θ, the alongshore velocity v, the streamfunction for the across-shelf flow ψ, two times the turbulent kinetic energy q^2, and the vertical turbulent kinematic viscosity K_M from the Q experiment at days 15, 25, and 35. All variables are averaged over an inertial period. The contour intervals are $\Delta\sigma_\theta = 0.2$ kg m^{-3}, $\Delta v = 0.1$ m s^{-1}, $\Delta\psi = 0.1$ m^2 s^{-1} ($\psi = \pm 1.0$ and 0 m^2 s^{-1} bold and positive ψ dashed), $\Delta q^2 = 2 \times 10^{-4}$ m^2 s^{-2} ($q^2 = 10^{-3}$ m^2 s^{-2} bold), and $\Delta K_M = 4 \times 10^{-3}$ m^2 s^{-1} ($K_M = 2 \times 10^{-2}$ m^2 s^{-1} bold). Dotted line in the σ_θ plots indicates the depth of a mixed layer defined by $\Delta\sigma_\theta = 0.05$ kg m^{-3} from the surface to the base of the mixed layer.

in the initial conditions has strengthened considerably. Across-shelf circulation shown by the streamfunction ψ indicates offshore Ekman transport near the surface and onshore return flow concentrated in a bottom boundary layer. A front in the alongshore velocity has developed 10–12 km offshore. In the same location, an abrupt thickening of the surface boundary layer occurs as near-surface streamlines for the offshore flow experience a dramatic downward excursion as they cross the frontal region. These frontal features are present to some extent in the experiments in Part 1, forced with a constant wind stress, but are much more prominent here (see, e.g., Part 1, Fig. 5). The largest values of turbulent kinetic energy $\frac{1}{2}q^2$ occur in the core of the alongshore jet 12–28 km from the coast. On day 25, during the period of light winds, the upper 10 m of the water column has restratified due to onshore advection and surface heating. Alongshore jet velocities have slackened and no sharp velocity front is seen. The across-shelf circulation shows weak upwelling with complicated structure. A small counterrotating cell has developed in the lower water column 12–16 km offshore. Turbulent kinetic energy is low. On day 35, alongshore velocities have a maximum value close to those on day 15, but the core of the jet has widened and moved offshore and the velocity front is absent. The surface mixed layer has deepened. The across-shelf circulation is weaker than that seen on day 15, reflecting the lighter wind stress. On days 15 and 35, turbulence q^2 values are elevated throughout the top and bottom boundary layers apparently associated with the regions of largest vertical shear in v.

We note that the major qualitative difference between the $Q_{\nabla\times\tau}$ experiment with wind stress curl and the Q experiment is the sharpness of the alongshore velocity front on day 15. In $Q_{\nabla\times\tau}$, the velocity front is about twice as wide as in the Q experiment. The jet tends to be more symmetric and is centered about 20 km offshore. Even though the velocity front is wider in $Q_{\nabla\times\tau}$, the across-shelf circulation is very similar in the two experiments, both exhibiting the sharp jump in mixed layer depth through the frontal region.

Further details of the model's response to the first strong wind event can be seen in Fig. 4, which shows the σ_θ, v, ψ, q^2, and K_M fields from experiment Q on days 12, 14, and 18. The strongest forcing occurs on days 13 and 14, with a sustained wind stress of about 3 dyn cm^{-2}. Prior to the strongest winds, on day 12 the model σ_θ and v fields look similar to the initial conditions (Fig. 2). Across-shelf circulation is orderly, with offshore flow in a thin surface layer and onshore flow distributed uniformly through the interior. The day 14 fields show sharply upwelled isopycnals and a surface mixed layer that increases in depth toward the coast to a maximum depth of about 40 m, 10 km offshore. The across-shelf circulation is nearly three times stronger than on day 12, and the onshore return flow has become more concentrated in a bottom boundary layer. The surface boundary layer defined by the offshore flow shows an increase in thickness between 8 and 12 km offshore. This feature develops into an abrupt jump by day 15 (Fig. 3). The sharp front in v, which is seen on day 15 (Fig. 3), is not yet fully developed on day 14, suggesting that relaxation of the wind stress contributes to its development. This might explain why such sharp velocity fronts were not seen in Part 1, where the wind stress was held constant. Dynamics of the frontal development will be discussed in section 3c. Between days 15 and 18, under a weaker but still upwelling favorable wind stress, velocites in the alongshore jet are slightly reduced and the jet's inshore edge moves farther offshore. The across-shelf circulation responds quickly to the weakening wind stress after day 14, and by day 18 is devoid of structure.

b. Model responses from all experiments

Shown in Fig. 5 for the Q experiment are geostrophic velocities (v_G) computed from the model density [referenced to model v at middepth, as described in Part 1, Eq. (4.3)] and the absolute value of the difference, $|v - v_G|$. Although the geostrophic velocity field looks much like the total velocity field in Fig. 3, the alongshore velocity field deviates from the geostrophic velocity by up to about 5 cm s^{-1} in the interior on days 15 and 25 (note the different contour levels for v and $|v - v_G|$). By day 35, the alongshore jet is in geostrophic balance almost everywhere except in the surface and bottom boundary layers, similar to the results from the constant wind forcing cases in Part 1. The nongeostrophic component is introduced by the high-frequency component of the wind stress; by comparison, the $|v - v_G|$ fields from the $Q_{\tau_{lp}}$ experiment (Fig. 5) show that a nearly geostrophic jet is produced outside of the boundary layers on all three days. Analysis of the balance of terms in Q shows that the nongeostrophic component of v in the interior is balanced by the time derivative of u. In the surface boundary layer, the nongeostrophic v is balanced by both the time derivative and the nonlinear advection, and in the bottom boundary layer, v is negligible compared to advection and diffusion.

Sixty-day averages of the σ_θ, v, ψ, and q^2 fields from experiments NQ, Q, $Q_{\tau_{lp}}$, and Q_{ifi} are shown in Fig. 6. The main differences between the Q and NQ experiments are the lower near-surface density gradients and the deeper surface boundary layer (shown by the ψ and q^2 fields) in NQ. The streamlines for the NQ and Q experiments indicate similar offshore transport despite the differences in surface mixed layer depth. The upwelling into the surface layer primarily occurs close to the coast through the bottom boundary layer. The use of low-pass filtered wind stress in $Q_{\tau_{lp}}$ produces mean fields nearly identical to those of Q, except for slightly lower surface values of q^2 and small differences in the across-shelf circulation. For Q_{ifi}, initialized with level

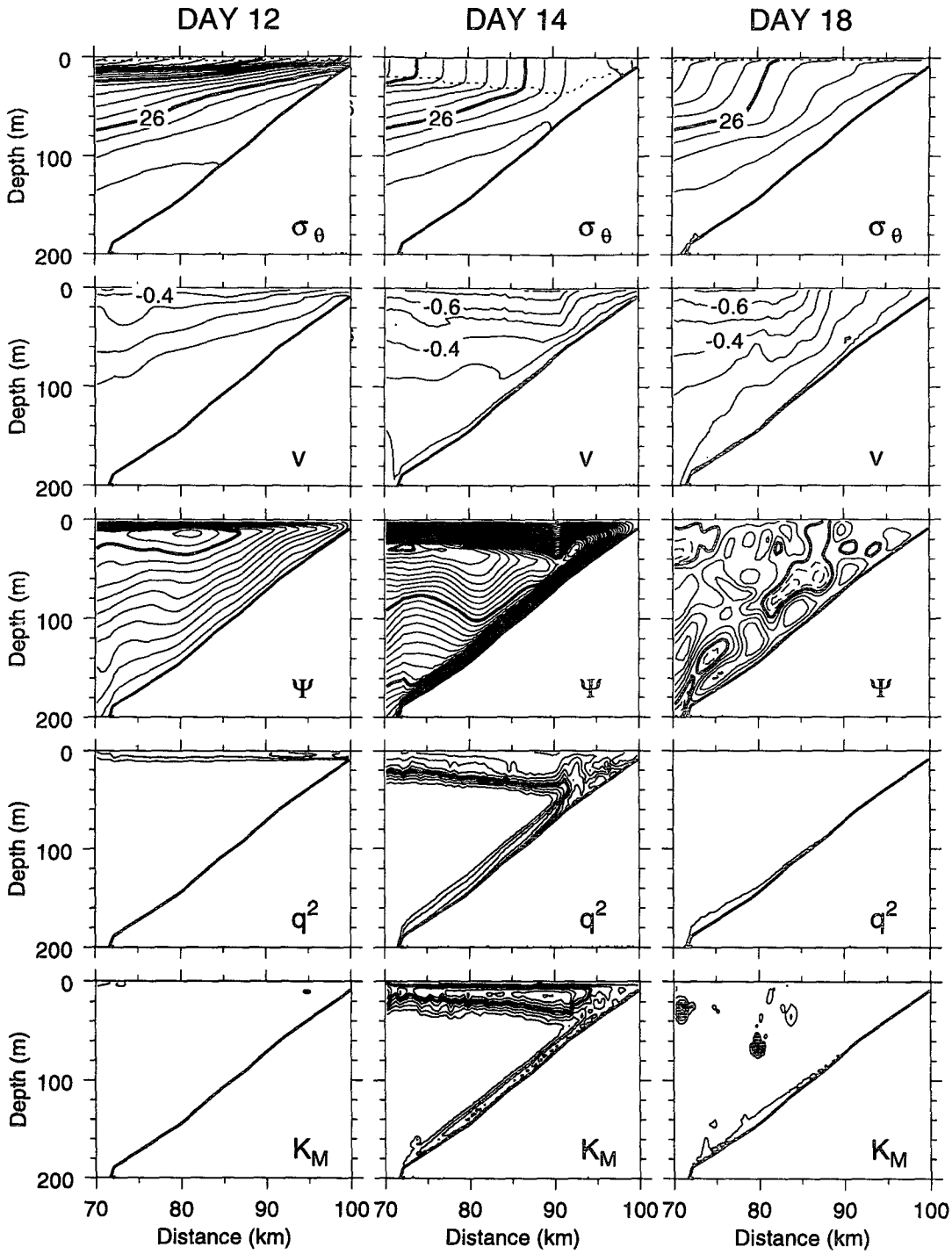

FIG. 4. Fields from the Q experiment at days 12, 14, and 18. Contour intervals as in Fig. 3.

isopycnals and zero velocities, the mean stratification is higher and the alongshore velocity jet is much narrower, similar to the jet in the basic-case experiment of Part 1. This demonstrates that in Q the wider jet prescribed by the initial density field persists and defines the jet scale through the entire 60-day run. The mean across-shelf circulation in Q_{ifi} shows somewhat more upwelling of fluid into the surface layer from the interior over the shelf.

For a better perspective on the time evolution of the model fields, σ_θ, v, u, and q^2 from the Q experiment are contoured as functions of time and depth at the

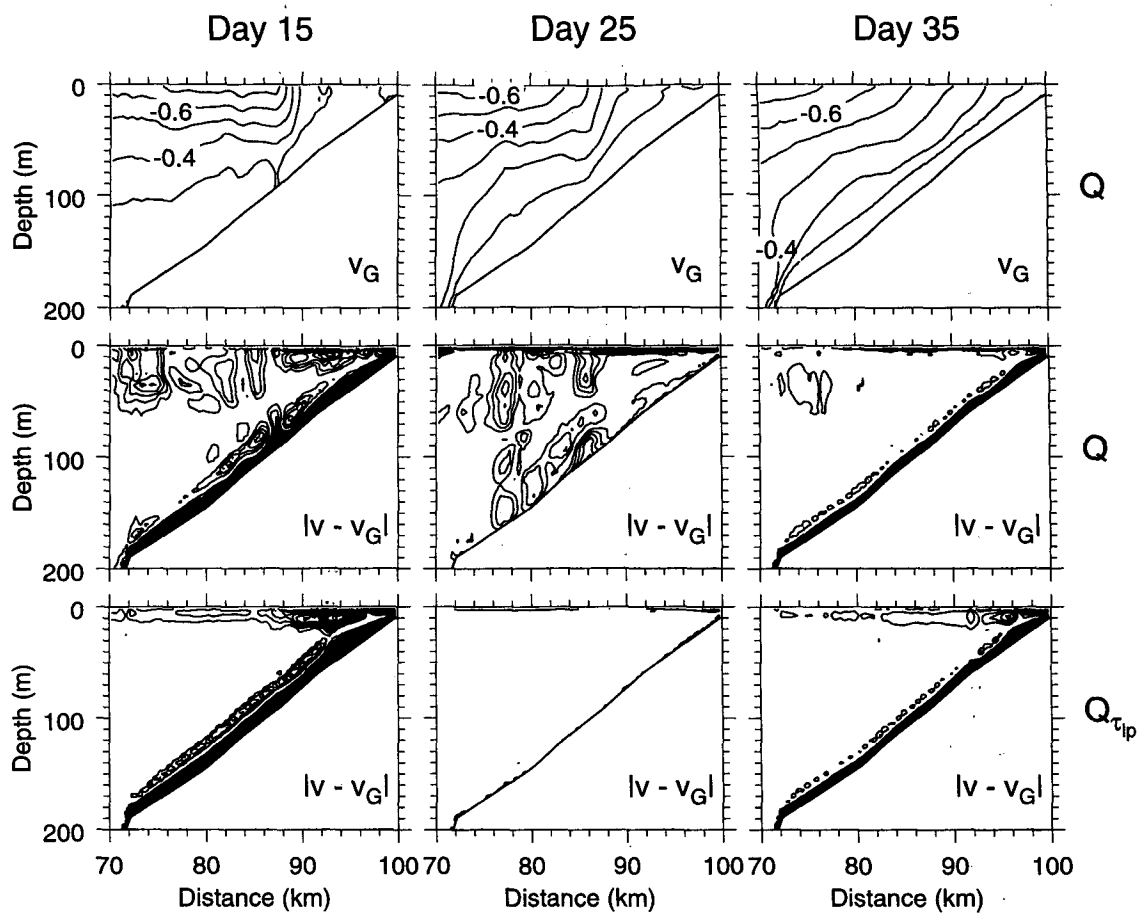

FIG. 5. Geostrophic alongshore velocity v_G, computed from σ_θ (referenced to model v at middepth) from the Q experiment, and the difference $|v - v_G|$ for experiments Q and $Q_{\tau_{lp}}$. Contour intervals are $\Delta v_G = 0.1$ m s^{-1} and $\Delta|v - v_G| = 0.01$ m s^{-1}.

100-m isobath in Fig. 7. The time variation of σ_θ shows that the stratification erodes dramatically during the first upwelling event and is only partly regenerated by the surface heating. Alongshore velocities are spun up over the whole water column on days 13–14 and relax slowly over a 5–8-day period when the wind dies down on day 15. The across-shelf velocity u develops a complicated structure in the interior between days 15 and 30, characterized by variations on vertical scales of 10–30 m and timescales of 3–6 days. This structure in u is related to the nongeostrophic component of v shown in Fig. 5. Elevated values of turbulent kinetic energy are found throughout the surface and bottom boundary layers, corresponding closely to the regions where the across-shelf flow is largest. Similar plots of the u velocities from the NQ, $Q_{\tau_{lp}}$, and Q_{τ_N} experiments are shown in Fig. 8. A deeper surface boundary layer develops in NQ in response to the first wind event around day 13. As a consequence, near-surface offshore velocities on days 25–40 extend to a greater depth and are much smaller in NQ than those seen in the experiments with surface heating. The bottom boundary layer is virtually unaffected by surface heating. The across-shelf circulation between days 15 and 30 of the NQ experiment exhibits complex structure in the interior, as seen in the Q experiment. Forcing with either low-pass filtered buoy B wind stress in $Q_{\tau_{lp}}$ or the weaker hourly Newport wind stress in Q_{τ_N} has the effect of nearly eliminating this small-scale structure. While $Q_{\tau_{lp}}$ produces flow in the boundary layers very similar to that produced by experiment Q, u velocities in the interior between days 15 and 30 are nearly zero. In Q_{τ_N}, the surface boundary layer transport is noticeably smaller and the interior flow is weaker.

As a concise way of comparing the major features of the various experiments, profiles of the 60-day averaged fields of u, v, σ_θ, q^2, and K_M at the 100-m isobath are shown in Fig. 9. The NQ experiment has a deep (60 m) mean surface turbulent boundary layer, with K_M values nearly four times larger than those from Q (note the difference in scale for K_M). The depth of this surface boundary layer is about three times greater than the mean boundary layer in Q (25 m) and the observed boundary layer (approximately 20 m) defined by the zero crossing of the observed mean u velocities (see Figs. 15 and 16). The experiment $Q_{\tau_{lp}}$ gives results

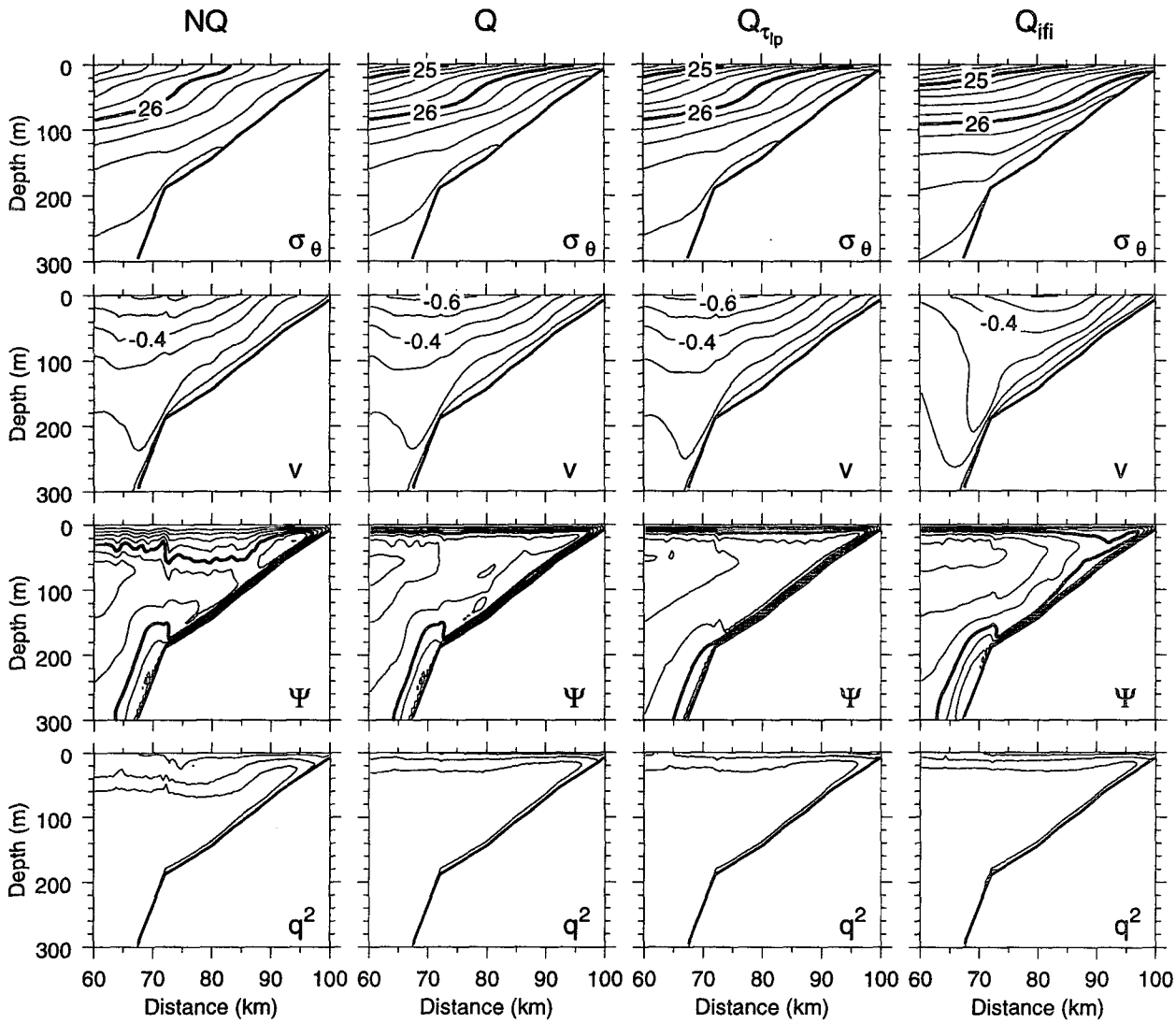

FIG. 6. Sixty-day averaged fields of σ_θ, v, ψ, and q^2 from experiments NQ, Q, $Q_{\tau_{lp}}$, and Q_{ifi}. Contour intervals are $\Delta\sigma_\theta = 0.20$ kg m^{-3}, $\Delta v = 0.1$ m s^{-1}, $\Delta\psi = 0.05$ m^2 s^{-1} ($\psi = -0.25$ m^2 s^{-1} bold), and $\Delta q^2 = 10^{-4}$ m^2 s^{-2}.

nearly identical to Q for these time-averaged variables, except that $Q_{\tau_{lp}}$ has smaller values of q^2 and K_M in the interior. Experiment Q_{τ_N} shows generally smaller across-shelf velocities and greatly reduced q^2 and K_M in the boundary layers. Inclusion of the alongshore pressure gradient (experiment $Q + P_y$) results in lower alongshore jet velocities and distribution of the across-shelf return flow in the interior, mostly between depths of 40 and 80 m, rather than in a bottom boundary layer. Compared to Q and $Q_{\tau_{lp}}$, turbulence levels near the bottom are reduced in Q_{τ_N} and in $Q + P_y$ due to the smaller velocities in the bottom boundary layer in those cases.

The depth-integrated offshore transport [defined as in Part 1, Eq. (4.2)] as a function of time and across-shelf distance is shown in Fig. 10 for the Q and $Q_{\nabla\times\tau}$ experiments. Predicted Ekman transports, $\tau^{(y)}/\rho_0 f$, from buoy B wind stress averaged over the preceding 24 hours are shown by the black bars. Since the model requires the vertically integrated across-shelf transport to be zero, local maxima in transport must represent recirculation in the (x, z) plane. Focusing first on the Q experiment, we see that during strong upwelling winds (days 15, 30, and 35), the transport increases rapidly in the region 0–6 km from the coast, to a value near the expected Ekman transport. Further increases sometimes occur out to around 30 km offshore. For example, on day 35, beyond 10 km offshore, surface layer transport continues to increase gradually across the shelf (see Fig. 3). It is notable that there are times, for example, on days 20 and 25, when the offshore transport over much of the shelf differs considerably

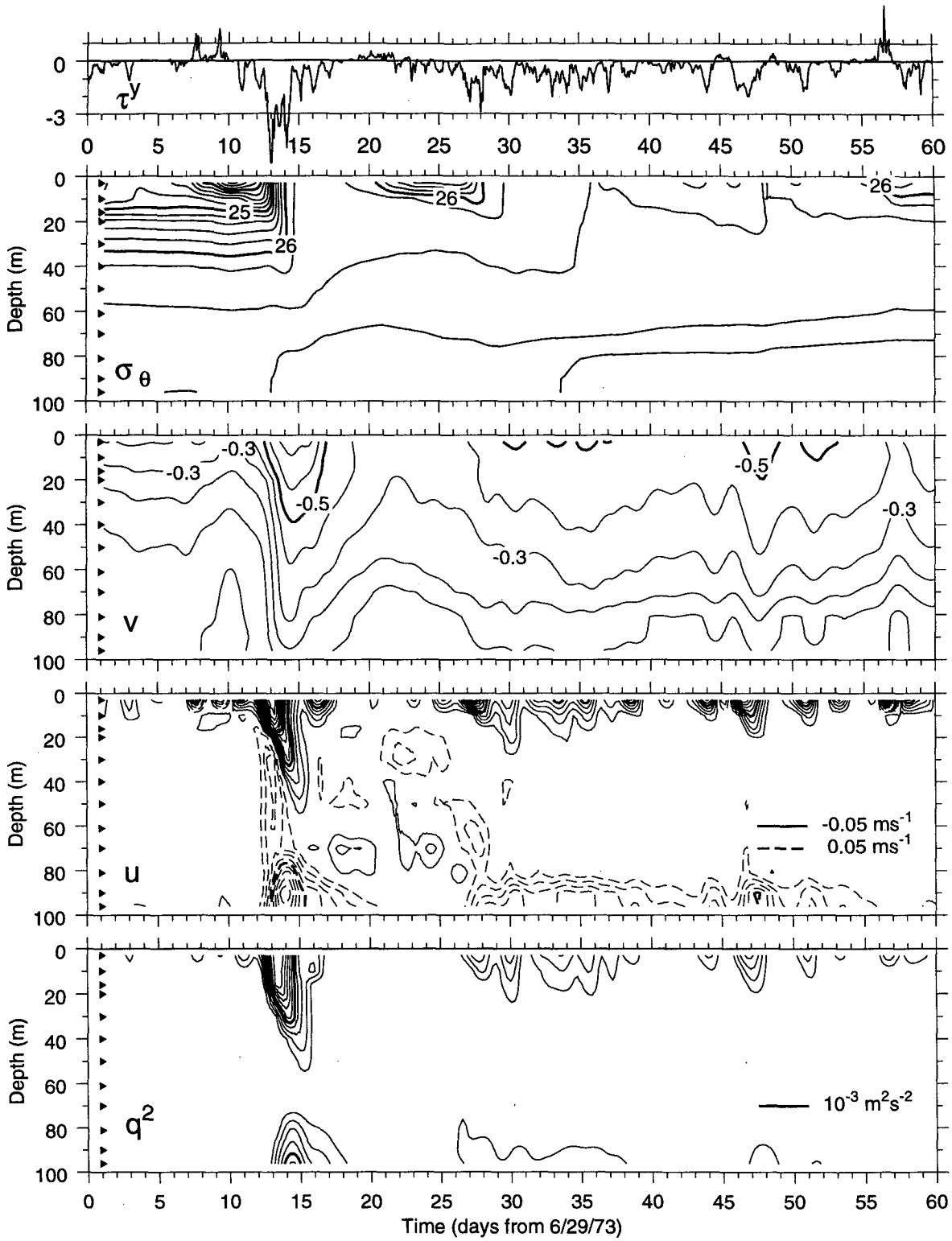

FIG. 7. Contours of σ_θ, v, u, and q^2 as a function of depth and time at the 100-m isobath from the Q experiment. The model outputs used are low-pass filtered hourly values at depths indicated by triangles. Contour intervals are $\Delta\sigma_\theta = 0.2$ kg m^{-3}, $\Delta v = 0.1$ m s^{-1}, $\Delta u = 0.01$ m s^{-1} (positive onshore velocities are dashed and $u = \pm 0.05$ m s^{-1} contours are bold, zero contour not shown), and $\Delta q^2 = 2 \times 10^{-4}$ m^2 s^{-2} ($q^2 = 10^{-3}$ m^2 s^{-2} bold). Hourly alongshore component of the buoy B wind stress (dyn cm^{-2}) is shown at the top.

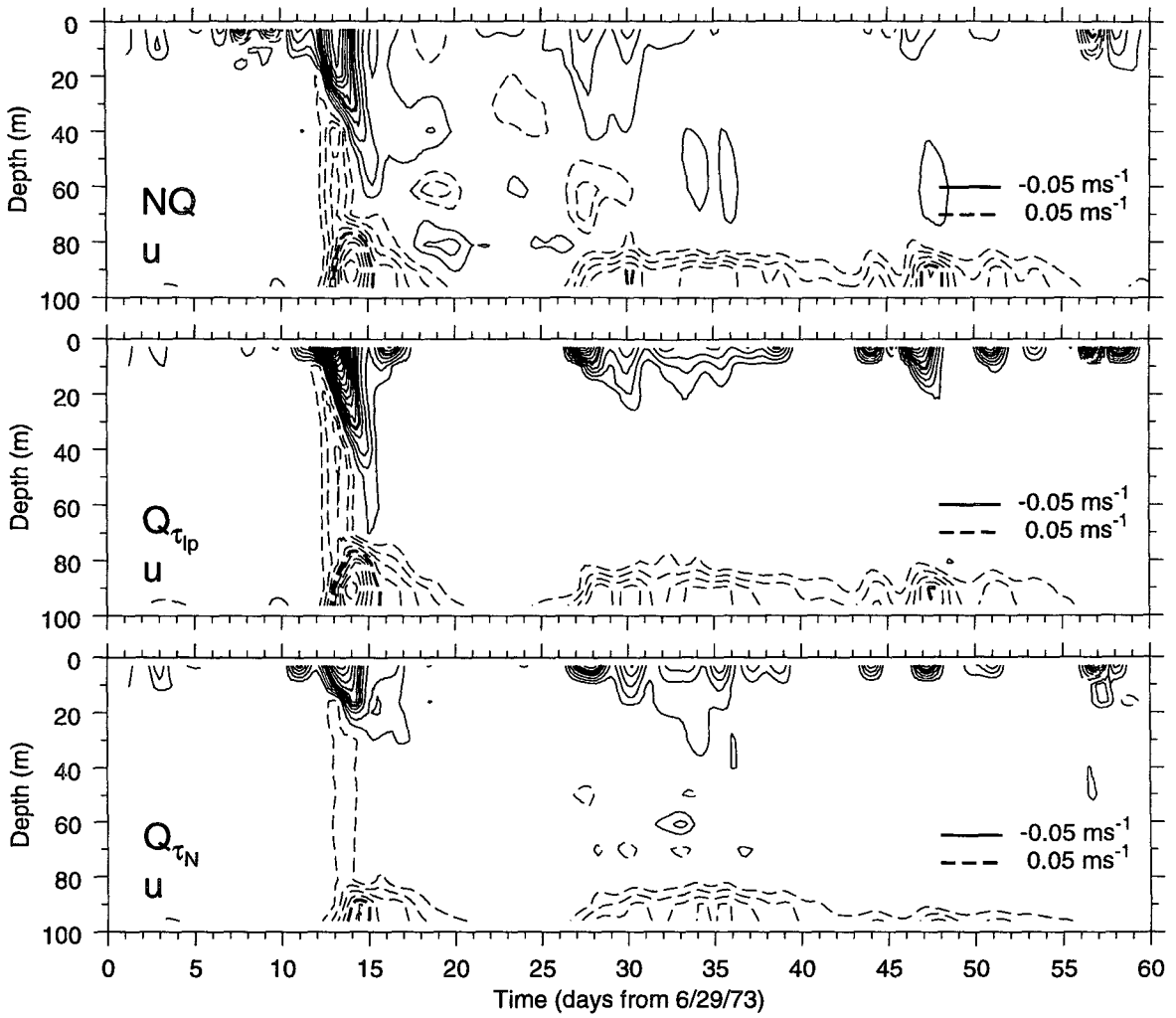

FIG. 8. Contours of u as a function of depth and time at the 100-m isobath for experiments NQ, $Q_{\tau_{lp}}$, and Q_{τ_N}. Contour intervals are $u = 0.01$ m s^{-1} (positive onshore velocities are dashed and $u = \pm 0.05$ m s^{-1} contours are bold, zero contour not shown).

from the Ekman value. This situation evidently results from complex across-shelf circulation patterns as shown in the ψ field on day 25 in Fig. 3. In the 60-day averages shown in the top panel, local maxima average out and model transport is very close to the predicted Ekman transport. The $Q_{\nabla\times\tau}$ experiment develops across-shelf transport distributed across the shelf much like in Q, suggesting that the horizontal scale over which the Ekman transport develops is determined more by the topography and presence of the coast rather than by a near-shore curl of the wind stress.

c. *Balance of terms from the Q experiment*

We examine the balance of terms in the alongshore momentum v equation [Eq. (2.1c) in Part 1] and in the density σ_θ equation [Eq. (2.1d) in Part 1] for experiment Q. The analysis of the balance of terms is first presented as a function of time at the 100-m isobath and then as a function of space on a near-surface across-shelf section for selected days. In Fig. 11, low-pass filtered time series of v and σ_θ equation terms are shown at depths of 3, 10, 20, 50, and 96 m at the 100-m isobath. Although the balances are strongly time dependent, each upwelling event sets up essentially the same balance of terms, varying primarily in magnitude and duration. Only the first upwelling event is shown. For the discussion here, we adopt the simplified notation used in Part 1 [Eq. (6.2)], where for example, v_t represents $H^{-1}\partial(vD)/\partial t$ [where $H(x)$ is bottom depth, $\eta(x, t)$ is surface elevation and $D = H + \eta$]. As in Part 1, the signs of v_t and $(\sigma_\theta)_t$ are positive and the sum of all terms equals zero. The horizontal diffusion terms are negligible in both the v and σ_θ equations.

In the v equation, at 3 m, the vertical diffusion term $-(K_M v_z)_z$ closely follows the time variation of the

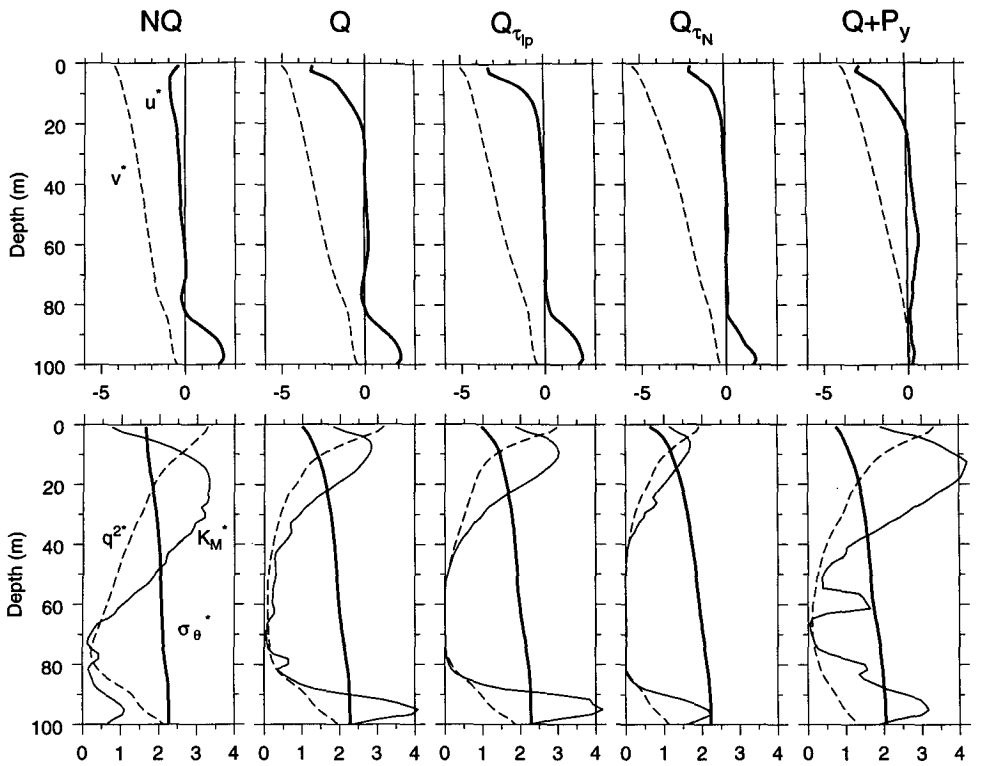

FIG. 9. Vertical profiles of the 60-day averages of u and v fields (upper panel) and σ_θ, q^2, and K_M fields (lower panel) at the 100-m isobath for experiments NQ, Q, $Q_{\tau_{lp}}$, Q_{τ_N}, and $Q + P_y$. The scaling is $u^* = u10^2$ m s^{-1}, $v^* = v10$ m s^{-1}, $\sigma_\theta^* = \sigma_\theta - 24.5$ kg m^{-3}, $q^{2*} = q^2 10^4$ m^2 s^{-2}, and $K_M^* = K_M 10^3$ m^2 s^{-1}. For NQ, the scaling for K_M is $K_M^* = K_M 250$ m^2 s^{-1}.

alongshore wind stress with opposite sign. It is almost completely balanced by the Coriolis force term fu, as in a linear Ekman layer. A similar balance but with the signs reversed is found at 96-m depth in the bottom boundary layer, only smoothed and slightly lagged in time. The acceleration v_t is generally much smaller than the vertical diffusion and Coriolis force terms. Nonlinear advection, $(uv)_x + (\omega v)_z$, generally varies in sign in the surface boundary layer and contributes significantly to the overall balance during and immediately following the strong wind event. Its role can be more easily understood in the across-shelf sections discussed below. In the interior, all terms are smaller. The acceleration of the alongshore jet at 50 m (the large negative v_t from days 12–16) is caused by a sequence of positive peaks in three different terms. On day 13, fu peaks, while u is part of the interior onshore flow (this can be seen in Fig. 7). On day 14 nonlinear advection reaches a maximum as the across-shelf flow changes direction to become part of the near-surface offshore flow. Finally, diffusion dominates on day 15 as the fluid at a depth of 50 m is engulfed by the deepening turbulent boundary layer, mixing down the faster (larger negative v) overlying water. The frictional response to the first upwelling event can be seen to propagate down to 50 m over a few days as the boundary layer deepens (also visible in the u and q^2 fields in Fig. 7).

In the σ_θ equation, the largest variation of terms occurs in the upper boundary layer, mostly above 20 m. The balance is primarily between $(u\sigma_\theta)_x + (\omega\sigma_\theta)_z$ and $(\sigma_\theta)_t$, reflecting advection of σ_θ with fluid particles. Vertical diffusion warms the water [i.e., positive diffusion causes negative $(\sigma_\theta)_t$] below the surface at the beginning of the first upwelling event (day 11 at 10 m and day 13 at 20 m) as the deepening mixed layer reaches first the 10 m then the 20-m level and warmer (less dense) water is mixed downward. Thereafter, advective cooling dominates. On day 13, vertical diffusion warms the water at 20 m and cools the water at 10 m, as temperatures in the mixed layer are equalized (as seen in the σ_θ field in Fig. 7). Diffusion is relatively weak after the initial wind event due to the diminished vertical density gradient. During the second strong wind event on days 27–38, the density response is much weaker, consisting primarily of a short 2–3-day pulse of advective cooling. As found by Rudnick and Davis (1988) for the CODE region, the surface heat flux is not important in the fluctuating heat balance.

Across-shelf sections of terms in the v momentum and σ_θ equations from experiment Q are shown in Fig. 12 for days 14, 15, and 35. Terms are displayed along

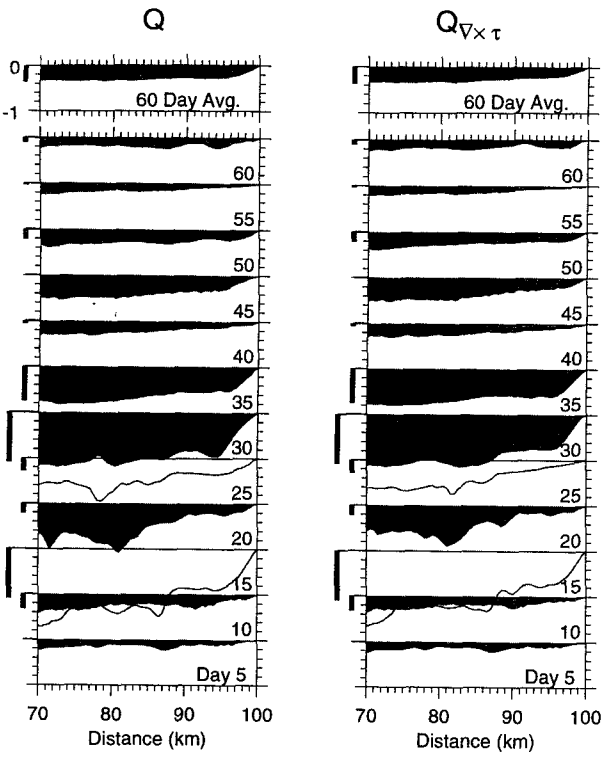

FIG. 10. The net offshore transport $U_{(-)}$ ($m^2\ s^{-1}$) as a function of x every five days for experiments Q and $Q_{\nabla\times\tau}$. Labels on the curves are time in days. The large ticks on the vertical axis represent a transport of 1 $m^2\ s^{-1}$. The solid bars to the left of each curve indicate the predicted Ekman transport $\tau^{(y)}/\rho_0 f$ calculated by time averaging the buoy B alongshore wind stress over the preceding 24 hours.

the $\sigma = -0.11$ level, which varies from a depth of 1.2 m at the coast to 26.3 m at 30 km offshore. In the v momentum equation, the positive vertical friction term near the surface acts to accelerate the southward jet (produce a negative v_t), and the Coriolis term generated by the offshore flow (negative fu) tends to decelerate the jet (produce a positive v_t). These terms nearly balance across the shelf, and both exhibit an offshore minimum near 10 and 12 km from the coast on days 14 and 15, respectively, corresponding to the locations of the maximum thickness in the surface boundary layer. With the near balance of $-(K_M v_z)_z$ and fu, nonlinear advection appears to determine the acceleration of the flow v_t even though advection is usually smaller in magnitude than those other two terms. On day 14, nonlinear advection produces deceleration of v (positive v_t) inshore of 12 km, and positive acceleration of v (negative v_t) offshore of 22 km. This balance basically represents advection of the jet core offshore. On day 15, the jet is decelerating (positive v_t offshore of 10 km) even though the wind stress is still upwelling favorable. This deceleration of the jet velocities is apparent in Figs. 3 and 4, on days 14 and 15. Although the vertical friction is contributing to acceleration of the jet, offshore flow near the surface is so strong that the combined Coriolis and nonlinear advection terms dominate to produce a positive v_t. The nonlinear advection term has a large peak 10–12 km offshore on day 15 due to the maximum in v_x in the alongshore velocity front. On day 35, vertical friction causes acceleration of v inshore of about 12 km offshore and the Coriolis and nonlinear terms decelerate the jet in the region 12–26 km offshore.

In the σ_θ equation on each of the three days shown in Fig. 12, the balance at distances greater than about 12 km from the coast is primarily advective cooling, that is, negative nonlinear advection producing positive $(\sigma_\theta)_t$. Diffusion cools the surface waters near the coast as the cooler underlying water is mixed upward. On day 14, the advection term is large and negative offshore of about 8 km but switches sign inshore due to advection of a pocket of warm water near the coast. Still, inshore of 8 km cooling by vertical diffusion prevails. On day 15, advective cooling dominates both offshore and inshore of the alongshore velocity front, while warming occurs 6–12 km offshore due primarily to advection offshore (and vertical mixing) of the warmer water near the coast.

Over a 60-day time average, the model exhibits net cooling (increase in density) over the shelf below about 3 m. Profiles from the Q experiment of 60-day averages of terms in the σ_θ equation at the 100-m, 60-m, 40-m and 20-m isobaths are shown in Fig. 13. The signs of the terms are the same as in Fig. 12. The net cooling is due primarily to advection and is greatest in the surface boundary layer at the 60-m and 100-m isobaths. Near the surface, the advective cooling term is reduced by the effects of vertical diffusion and by the solar radiation term, which was relatively small in the instantaneous balance. For comparison, corresponding profiles from the Q_{ifi} experiment are also shown in Fig. 13. Initializing with level isopycnals causes a large increase in the advective cooling term throughout the interior. This point is discussed further in section 4.

Bryden et al. (1980) estimated mean and eddy advective heat flux using the temperature and horizontal components of velocity measured at the CUE-2 moorings. Using Bryden's method, we compute corresponding fluxes using time series from the Q experiment. Mean heat flux is calculated from hourly time series of model output as

$$\mathrm{MHF} = -(c_p/\alpha)\int_{-100}^{0} (\bar{u} - \langle\bar{u}\rangle)(\overline{\sigma_\theta} - \langle\overline{\sigma_\theta}\rangle)\,dz \tag{3.1a}$$

and "eddy" heat flux as

$$\mathrm{EHF} = -(c_p/\alpha)\int_{-100}^{0} \overline{(u - \bar{u})(\sigma_\theta - \overline{\sigma_\theta})}\,dz, \tag{3.1b}$$

where the bar indicates a time average and brackets indicate depth average. The specific heat at constant pressure $c_p = 3996\ J\ kg^{-1}\ K^{-1}$ and the coefficient of

thermal expansion $\alpha = 2.734 \times 10^{-4}$ K^{-1}. A profile of the resultant mean and eddy heat flux at the 100-m isobath for experiment Q is shown in Fig. 14. Bryden finds that at the 100-m isobath the depth-integrated eddy component is 40% of the mean. For the Q experiment, the eddy component is 30%–40% of the mean only in the upper 16 m, and when depth-integrated over 100 m, is only 1% of the mean. Send (1989), interpreting Bryden's result in light of heat flux analysis from the CODE region, suggests that eddy heat flux on the Oregon shelf is due primarily to wind variability. Our result suggests that the eddy contribution in Bryden et al. (1980) has another origin.

4. Comparison with observations

Contours of the observed temperature and velocities from the Carnation and buoy B moorings as a function of time and depth are shown in Fig. 15. The observed temperature stratification is remarkably resilient over the entire 60 days, recovering quickly from periods of destratification, notably on days 14–16, 31–35, and 47–49. The corresponding density field from the Q experiment (Fig. 7) shows that the model starts out highly stratified, but after mixing down to over 40-m depth on day 15, it never regenerates the same near-surface stratification, particularly at depths of 20–40 m. Although salinity is important here so that density and temperature cannot be directly compared, further comparisons between model densities and CTD densities support this suggested difference in stratification.

The model reproduces both the vertical shear and the surface values of the alongshore velocities reasonably well, except during some flow reversals that are unrelated to the local wind. The observed alongshore velocities generally exhibit greater time variability than the model output. Autocorrelation timescales of the observed v velocities are 2–3 days (Table 2), whereas the model has timescales of 3–4 days. In comparison to the v's from the Q experiment, the observed v field

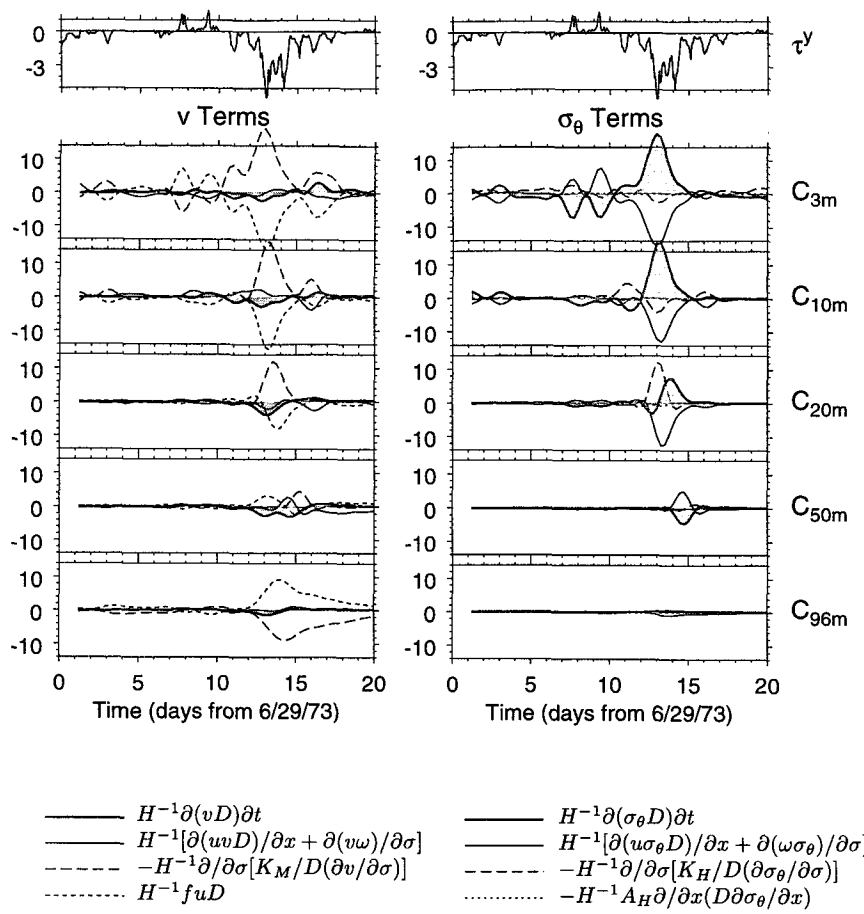

FIG. 11. Balance of terms for five depths at the 100-m isobath. On the left-hand side are low-pass filtered terms in the v momentum equation. Units are 10^{-6} m s^{-2}. On the right-hand side are low-pass filtered terms in the σ_θ equation. Units are 10^{-6} kg m^{-3} s^{-1}. The time derivative terms are shaded. Hourly alongshore component of the buoy B wind stress (dyn cm^{-2}) is shown at the top.

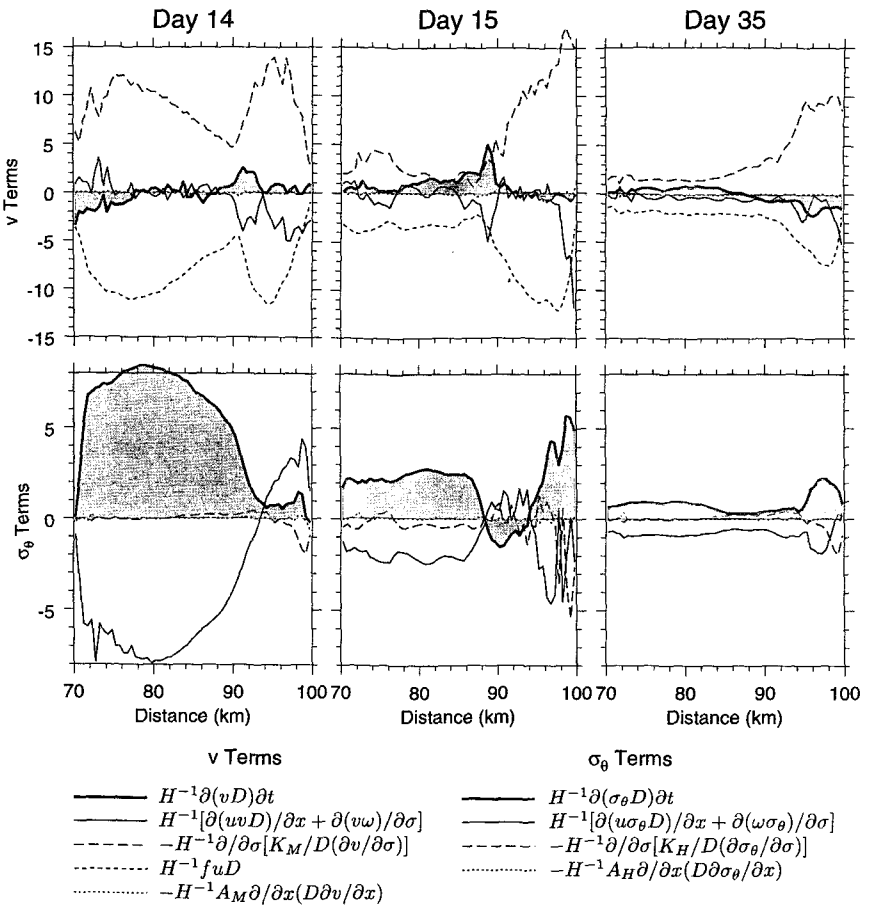

FIG. 12. Across-shelf variation of near-surface ($\sigma = -0.11$) terms averaged over an inertial period on days 14, 15, and 35 for the v momentum equation (upper row) and σ_θ equation (lower row). Line types and units are the same as in Fig. 11, with the addition of the horizontal diffusion term in the v momentum equation. The time derivative terms are shaded.

responds more quickly and more strongly to initiation of the two main upwelling events and decelerates more quickly when the winds relax (days 16–17 and 39–41). Model response to the second upwelling event is sluggish by comparison, probably due to the diminished stratification. There are indications in the observations of nearly barotropic, depth-independent events unrelated to the local wind. For example, on days 30–34 the alongshore velocities are reduced to near zero even during sustained upwelling winds. The observed current fluctuations are evidently associated with wind forcing at locations south along the coast and propagation northward of coastally trapped waves. This conclusion is supported by the results that sea level fluctuations at Newport during CUE-2 are highly correlated with predictions from the forced first-order wave equation (Halliwell and Allen 1984) and that coastal sea level is highly correlated with the alongshore currents (Kundu et al. 1975).

The observed across-shelf velocities (Fig. 15) exhibit much stronger fluctuations than those from the Q model (note the difference in contour levels between Fig. 15 and Fig. 7), and show that the observed surface offshore flow is mostly confined to the upper 20 m. The time-dependent depth-averaged velocity, $100^{-1}\int_{-100}^{0} u(z, t)dz$, is removed from the observed u field for the plot in Fig. 15 and for further statistical comparisons with the model (as in Dever and Lentz 1994). This depth-averaged velocity has a time mean and standard deviation of 0.011 ± 0.022 m s^{-1} and removes that part of the observed u velocity that this model, with a two-dimensional mass balance, cannot possibly reproduce. Autocorrelation timescales of the u field (Table 2) are generally similar for the observations and for the model (2.5–3.5 days). The observed u velocities show onshore flow between depths of 20 m and about 60 m but no onshore flow in a bottom boundary layer. This may be because the observed alongshore velocities near the bottom are generally poleward and would tend to produce offshore flow in the bottom boundary layer. In contrast to the observations, the Q model produces equator-

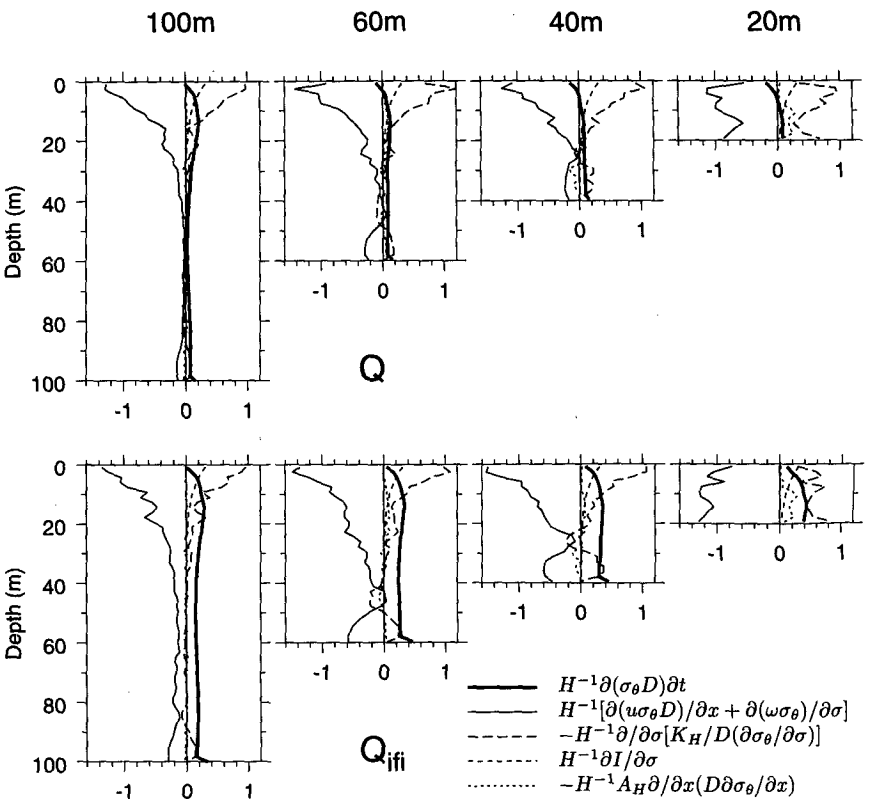

FIG. 13. Sixty-day time average of terms in the σ_θ equation at the 100-m, 60-m, 40-m, and 20-m isobaths from experiments Q (upper) and Q_{ifi} (lower). Units are 10^{-6} kg m^{-3} s^{-1}. A time derivative of 0.1×10^{-6} kg m^{-3} s^{-1} corresponds to $\Delta\sigma_\theta \approx 0.5$ kg m^{-3} over 60 days.

ward flow near the bottom and generally onshore flow in a bottom boundary layer.

Means and standard deviations of the velocity fields at the 100-m isobath are shown in Fig. 16 for the current meter measurements and for the Q, $Q + P_y$, Q_{ifi}, and Q_{τ_N} experiments. The model experiments all produce similar mean u profiles, and none reproduce either the large means or standard deviations observed in the u field. The vertical shear of the mean v field at mid-depth is well predicted by the Q model. For the Q and Q_{τ_N} experiments, the model mean v values are too strongly negative at all depths, and the standard deviations are somewhat lower than observed, especially for Q_{τ_N}. For the Q_{ifi} experiment, the mean v profile is much too strongly sheared and the standard deviation too large near the surface and too small below 60 m, reflecting the spinup of the coastal jet. Inclusion of the alongshore pressure gradient in $Q + P_y$ brings the mean v field close to the observations and improves prediction of the standard deviation of v; however, it gives no significant improvement in the u statistics.

Even after removing the depth-averaged u velocity, there are still large differences between the observed and model u velocities. The model's upper layer transport appears to be in an Ekman balance (Figs. 11 and 12) and yet Smith (1981) concludes that the observed surface layer transport is in agreement with an Ekman balance (but with an average magnitude of 1.7 times that predicted). In an attempt to understand the differences in model and observed transport, we compare the surface layer transport in the Q model with the predicted Ekman transport $\tau^{(y)}/\rho f$, and with the observed surface layer transport. There are several ways to define the depth over which u is integrated to estimate Ekman transport, and they produce substantial differences in transport. Smith (1981) uses a constant depth of 19 m, chosen from the zero crossing of the mean u profile at the 100-m isobath, whereas Lentz (1992), in his study of shelf boundary layers, integrates over a time-varying mixed-layer depth defined by a temperature difference of 0.05°C between the surface and the bottom of the mixed layer. The mixed-layer depth calculated using Lentz's definition is much shallower, having a mean of only 1.9 m and a maximum of 18 m. Lentz concludes that including the transport in a transition layer of approximately one-half the mixed-layer depth gives better agreement with predicted transport. Shown in Fig. 17 are time series of across-shelf transports at the 100-m isobath, predicted, produced by the model, and estimated from observations, illustrating the range of results. Predicted Ekman transport, $\tau^{(y)}/\rho f$, where $\tau^{(y)}$ is the low-pass filtered

buoy B wind stress, is shown in bold. Observed transport, calculated by integrating the observed u velocity (with the time varying depth-average removed) over the upper 19 m (referred to as Smith-TVDA), is also shown. Because the model time-dependent σ_θ fields do not yield a well-defined surface mixed layer, model transport from experiment Q is integrated over the top 25 m, a larger value than Smith's 19-m estimate to account for the model's deeper surface boundary layer (Fig. 16). Correlations between the predicted transport and all estimates of model and observed transport are significant, varying between 0.63 and 0.96 (Table 3). Estimates of mean transport vary greatly, depending on how the Ekman layer depth is chosen and whether the depth average of u is removed, and range from 56% to 208% of predicted. Figure 17 indicates that the time-varying model transport is in good agreement with the predicted Ekman transport. The observed transport is also in reasonable agreement (except for a few obvious events, for example on days 15–19) but depends on how the surface layer depth is chosen.

A comparison of observed and model mean density at the 100-m isobath is presented in Fig. 18. Profiles of the mean density and the initial density from the Q, $2Q$, Q_{ifi}, and $Q + P_y$ experiments are shown. The observed mean density is computed from 16 CTD profiles near the 100-m isobath: four profiles from each of four CUE-2 surveys covering model days 1–3, 12–16, 50–52, and 54–57. The observed mean density shows remarkably little evolution away from the initial profile and has very low variance below about 20 m. A slight cooling (density increase) occurs in the upper 25 m. In the Q experiment, σ_θ varies little at depths of 40–60 m, as observed, but increases substantially above 40 m and also in the lower 20 m, due to the effect of onshore flow in the bottom boundary layer. Doubling the surface heat flux (experiment $2Q$) has virtually no effect on the density structure below about 40 m, and even above 40 m, is insufficient to maintain the observed low density near the surface. Experiment Q_{ifi} shows a large increase in density throughout the water column, in contrast to the previous examples. As shown in Fig. 13, the cooling in the interior is primarily advective and is much larger in Q_{ifi} than in Q. Since the mean u velocity is similar in the Q and Q_{ifi} experiments (see Fig. 16), the difference in cooling can be attributed to the difference in orientation of the flow with respect to the isopycnals. In the Q experiment, the isopycnals are more parallel to the bottom, reflecting the initial conditions, and therefore more parallel to the across-shelf streamfunction (see Fig. 6) so the advective heat flux is smaller in Q than in Q_{ifi}. The $Q + P_y$ experiment shows a small net warming (density decrease) in the interior, mostly between depths of 40 and 70 m, where there is an onshore mean u velocity. The realistic low variance near the bottom is attributed to the lack of significant flow in a bottom boundary layer.

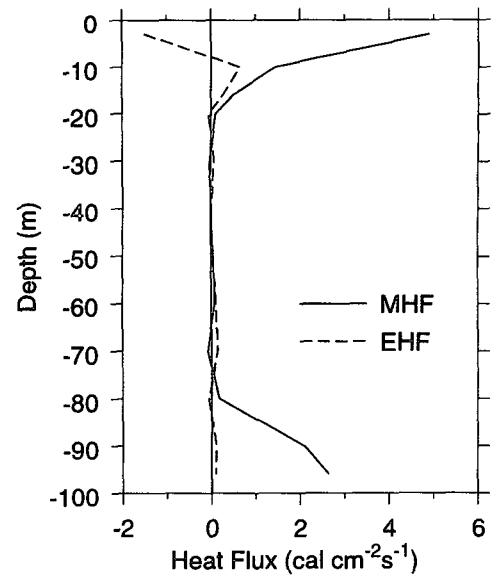

FIG. 14. Profiles at the 100-m isobath of mean (MHF) and eddy (EHF) contributions to the horizontal advective heat flux as defined in (3.1a,b) from the Q experiment.

Halpern (1976b) presents details of the time evolution of the near-surface stratification during the first upwelling event, using additional hydrographic surveys and time series of temperature at the buoy B mooring. In Fig. 19, time series of density at the 100-m isobath are shown for the Q and $2Q$ experiments, as well as for a 30-day experiment Q_t, forced with the daily average heat fluxes measured at buoy B during this period. Model densities are compared with temperature time series from the buoy B and Carnation moorings, plotted as in Halpern (1976b). Erosion of the model stratification in the upper water column on days 12–15 agrees well with the temperature observations; however, the model fails to restratify as quickly and as completely as the observations, irrespective of the magnitude and time variation of the surface heat flux. The ocean's retention of warm water in the upper 20 m in the face of strong offshore advection of cooler upwelled water implies that the heat budget is three-dimensional. The effect of the stronger surface heating ($2Q$) is obvious in the upper 20 m and negligible at 40 m.

Correlations between the current meter measurements, the model velocities from the Q experiment, and the alongshore wind stress are given in Table 2. Correlations of the Q experiment u velocities with observed u are significant in the top and bottom boundary layers and to a lesser extent at 40 and 60 m. Correlation of u with the wind stress $\tau^{(y)}$ is significant at all depths for the model experiments and at nearly all depths for the observations. For both model and observations, u velocities at and below 40 m are negatively correlated with the wind stress. Correlations of alongshore wind

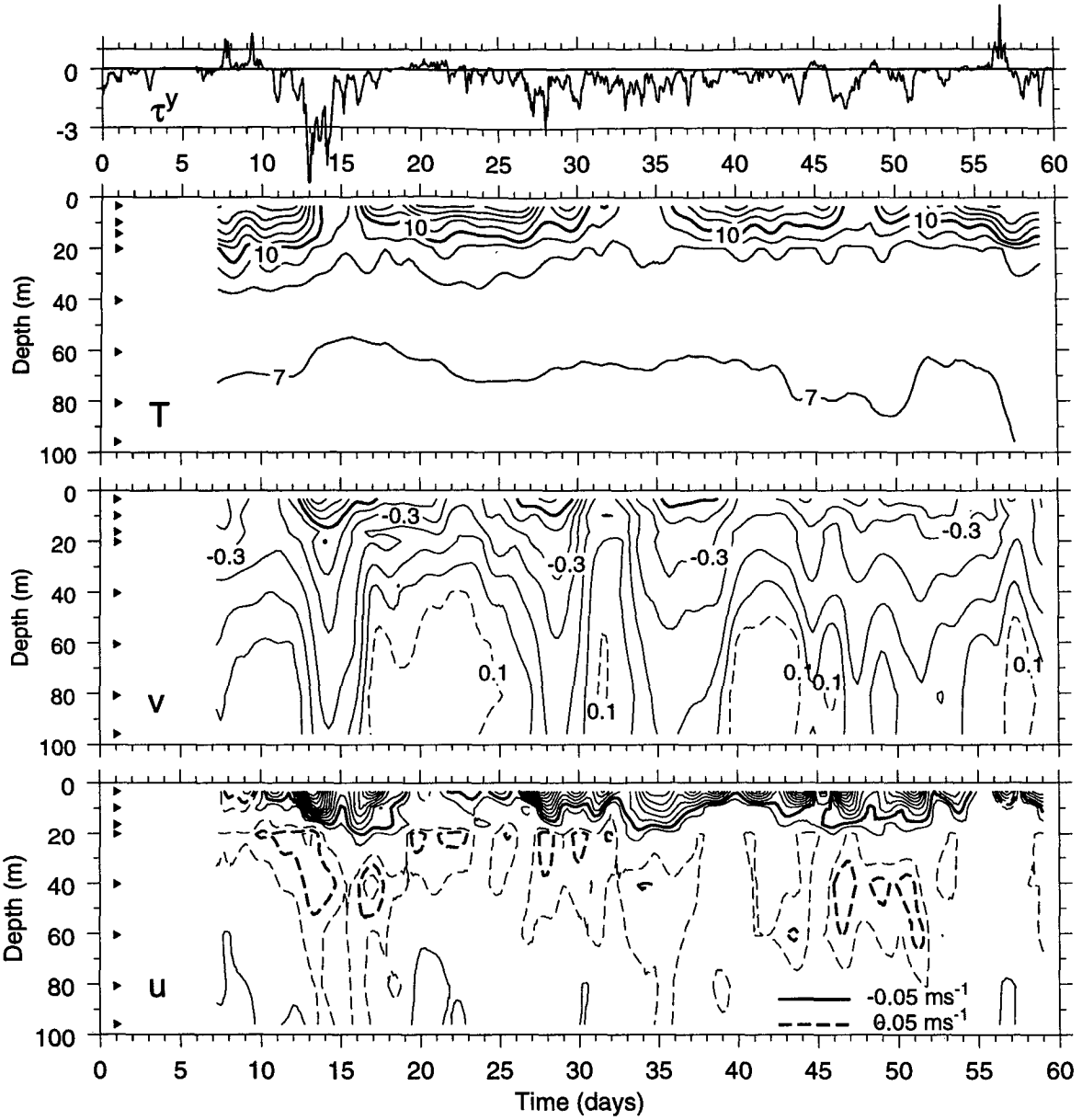

FIG. 15. Contours of observed temperature, v and u as a function of depth and time from current measurements at the Carnation and buoy B moorings (100-m isobath). The depth-averaged velocity has been removed from the observed u velocities. Contour intervals are $\Delta T = 1°C$, $\Delta v = 0.1$ m s^{-1} (positive northward velocities are dashed), and $\Delta u = 0.025$ m s^{-1} (positive onshore velocities are dashed and $u = \pm 0.05$ m s^{-1} contours are bold, zero contour not shown). The contour interval for u is different than in Fig. 7. Triangles indicate the measurement depths. The hourly alongshore component of the buoy B wind stress (dyn cm^{-2}) is shown at the top.

stress with both observed and model v velocities are significant at all depths. The correlations are higher, however, for the model and the maximum correlations occur at an additional lag of about 6 hours. The model v velocities are correlated with the observed v near the surface and the bottom, where both model and observations are most strongly correlated with the wind stress. The NQ experiment generally produces lower correlations with the observed velocities than the Q experiment. The $Q + P_y$ experiment produces correlations similar to those from the Q experiment. The higher standard deviations seen in the $Q + P_y$ v field (Fig. 16) are produced by very low-frequency variance and not by variance on the timescale of wind events. Regression coefficients of observed on model velocities show that the model underpredicts the near-surface u velocities (regression coefficients greater than unity) and overpredicts the near bottom u velocities. Regres-

TABLE 2. Correlations coefficients involving $\tau^{(y)}$ from buoy B, and the u and v velocities measured at the Carnation and buoy B moorings (u_0, v_0) and generated in experiment Q (u_m, v_m) at the 100-m isobath. Correlation coefficients between variables $\tau^{(y)}$ and u_0, for example, are denoted by C (τ^y, u_0) and the maximum lagged correlation coefficient (lag in hours) is listed. All correlation coefficients shown are significant at the 95% confidence level and those in bold are significant at the 99% level. Autocorrelation timescales in days, defined by the first zero crossing of the autocorrelation function, are also shown and are denoted for variable u_0, for example, by T (u_0). Regression coefficients (r) are obtained from regression of observed on model velocities.

Depth	Observations C (τ^y, u_0) (h)	T (u_0) (d)	Model C (τ^y, u_m) (h)	T (u_m) (h)	C (u_m, u_0)	r
3	**0.82** (0)	3.25	**0.89** (0)	3.5	**0.86**	2.00
10	**0.74** (6)	3.25	**0.77** (0)	2.75	**0.64**	1.58
16	—	2.75	**0.70** (6)	2.25	—	—
20	—	2.75	**0.71** (18)	2.75	—	—
40	**−0.59** (0)	3.75	**−0.40** (0)	3.25	0.24	0.61
60	**−0.51** (0)	3.5	**−0.82** (0)	2.5	0.37	1.01
80	**−0.55** (6)	3.25	**−0.80** (6)	1.25	—	—
96	**−0.63** (18)	3.0	**−0.89** (12)	4.25	**0.67**	0.63

Depth	Observations C (τ^y, v_0) (h)	T (v_0) (d)	Model C (τ^y, v_m) (h)	T (v_m) (h)	C (v_m, v_0)	r
3	**0.61** (12)	2.25	**0.83** (24)	3.25	0.61	1.01
10	0.49 (24)	2.25	**0.85** (30)	3.25	—	—
16	0.49 (24)	2.5	**0.85** (30)	3.25	—	—
20	0.53 (18)	2.5	**0.84** (30)	3.75	—	—
40	**0.61** (18)	3.0	**0.78** (30)	4.25	—	—
60	**0.69** (18)	3.0	**0.76** (24)	4.25	—	—
80	**0.72** (18)	3.0	**0.88** (18)	3.75	**0.62**	0.95
96	**0.72** (18)	3.0	**0.87** (24)	3.75	0.59	1.15

sion coefficients of the v velocities are close to unity where the model is correlated with the observations.

Across-shelf sections of σ_θ and alongshore velocities from the Q and $Q + P_y$ experiments compared with observed CTD densities and associated geostrophic alongshore velocities are shown for days 15 and 55 in Fig. 20. The magnitude of the model stratification above about 60 m is lower than observed by day 15 and remains too low through day 55. At day 15, both the Q model and observations show similar alongshore jets that extend across the entire shelf. The alongshore jet in the $Q + P_y$ experiment is somewhat narrower and a poleward countercurrent can be seen in the v fields near the shelf break. The basic structure of the alongshore jet seems to be better represented by the Q experiment than by $Q + P_y$, even though the maximum jet velocities in $Q + P_y$ are closer to those observed. By day 55, the model σ_θ and v fields no longer resemble the observed σ_θ and v fields, even though the v field from the $Q + P_y$ experiment has about the right magnitude over the shelf.

5. Discussion and summary

Results of these experiments have demonstrated the importance of including a surface heat flux in model simulations of coastal upwelling off the Oregon coast of longer than a few days. Also important is specification of realistic initial density and alongshore velocity fields, as these have a lasting effect on the structure of the alongshore current.

There are some substantial differences between the observed and the model density fields. One prominent feature of the observed density field is the stability and resiliency of the stratification at midshelf. The Q model density, in contrast, shows destratification and a significant increase in the upper 40 m. The observations show much greater offshore advection in the upper 20 m than does the model, which should result in greater advective cooling. Instead, it is the model that shows greater near-surface cooling, even with an additional buoyancy flux to simulate the effect of the Columbia River plume. This suggests a three-dimensional contribution to the observed advective heat flux, which may be partly due to variation in the location and strength of the plume. Some discrepancies may be due to shortcomings of the turbulence model. For example, the Mellor–Yamada level 2.5 turbulence model is known to produce shallower mixed layers than observed (Martin 1985). This particular feature, however, would not account for the excessively deep mixed layer produced by the model on day 14 (Figs. 7 and 15) and probably could not account for the excessive cooling over most of the water column seen in Fig. 18. Model tests indicate that the inertial-period averaged results are not sensitive to the details of the heat flux forcing. Use of a constant flux rather than a diurnal cycle of heating has no noticeable effects on the averaged fields. Also, using the time-varying daily averaged heat flux produces results very similar to using a constant daily average. Model results are also not appreciably affected

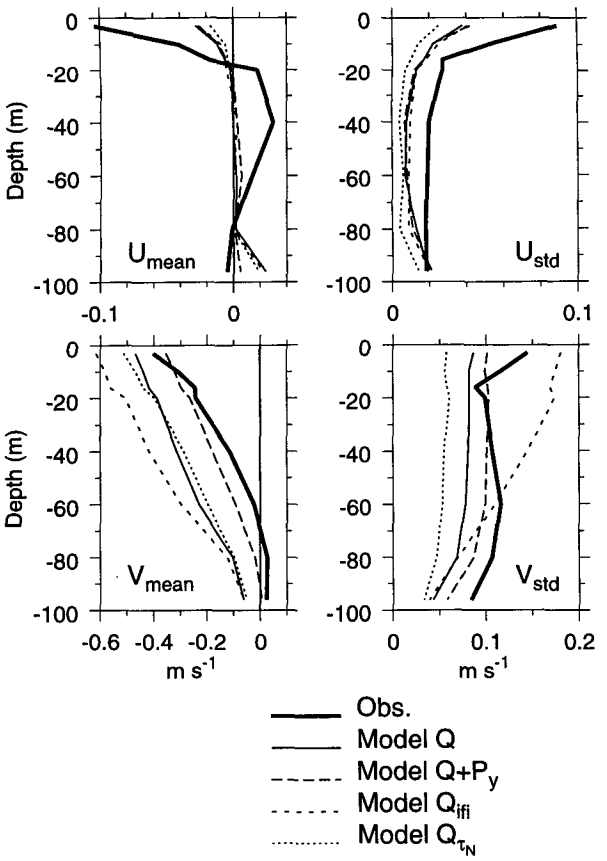

FIG. 16. Means and standard deviations of low-pass filtered time series of model-produced and observed u and v velocities at the 100-m isobath. Depths are the same as in Table 2.

by allowing deeper penetration of the solar radiation, as found by using Jerlov (1976) type I coefficients.

Imposing a constant alongshore pressure gradient improves the simulation of certain features, including the magnitude of the mean alongshore velocity field and lack of flow in the bottom boundary layer but does not significantly improve the correlation of the model

TABLE 3. Estimates of Ekman transport, predicted, observed (calculated three different ways), and model generated. Correlations are maximum lagged (lag in hours), and regression is observed (or model) on the predicted. Units are m^2 s^{-1}.

	Transport mean ± std dev	Correlation w/predicted	Regression coefficient
Predicted $\tau^y/(\rho_0 f)$	−0.45 ± 0.69		
Observed			
Smith (1981)	−0.67 ± 1.14	0.63 (6)	1.04
Smith-TVDA	−0.94 ± 0.96	0.78 (6)	1.08
Lentz (1992)	−0.25 ± 0.41	0.87 (0)	0.74
Model Q	−0.30 ± 0.46	0.96 (0)	0.64

produced velocities with the observed flow field. As was found by Chen and Wang (1990) for the CODE region, the two-dimensional model used here does not do well at reproducing the across-shelf flow below the mixed layer. Inclusion of a constant alongshore pressure gradient fails to produce the large interior across-shelf flow that was observed in the mean u field (Fig. 18), even after removing the depth average from the observed u field. It is interesting to note that Zamudio and López (1994) found that including a time- and space-varying alongshore pressure gradient had very little effect on the across-shelf flow, except to reduce the standard deviations of both the u and v velocities.

Results of the various wind-forcing tests indicate the advantage of using buoy wind measurements instead of shore-based wind measurements, as the more energetic buoy winds produce more realistic variances in the velocity fields. The high-frequency energy in the hourly wind forcing affects the details of the across-shelf circulation but does not qualitatively alter the low-frequency behavior of the density and alongshore velocity fields. Forcing with a wind stress that diminishes near the shore, consistent with the observed wind, has very small effects on the flow fields, except to reduce the strength of the front in alongshore velocity following the strong upwelling on days 13–14.

The observed three-dimensionality of the CUE-2 flow field is undoubtedly responsible for some of the

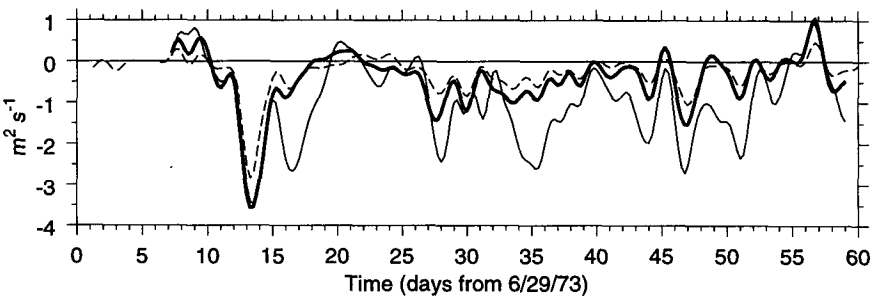

FIG. 17. Across-shelf transport in the surface boundary layer at the 100-m isobath. The heavy line indicates predicted Ekman transport $\tau^{(y)}/\rho_0 f$ from buoy B low-pass filtered wind stress, light solid line shows observed transport in the upper 19 m with depth-averaged u removed (Smith-TVDA), and the dashed line shows transport from experiment Q in the upper 25 m.

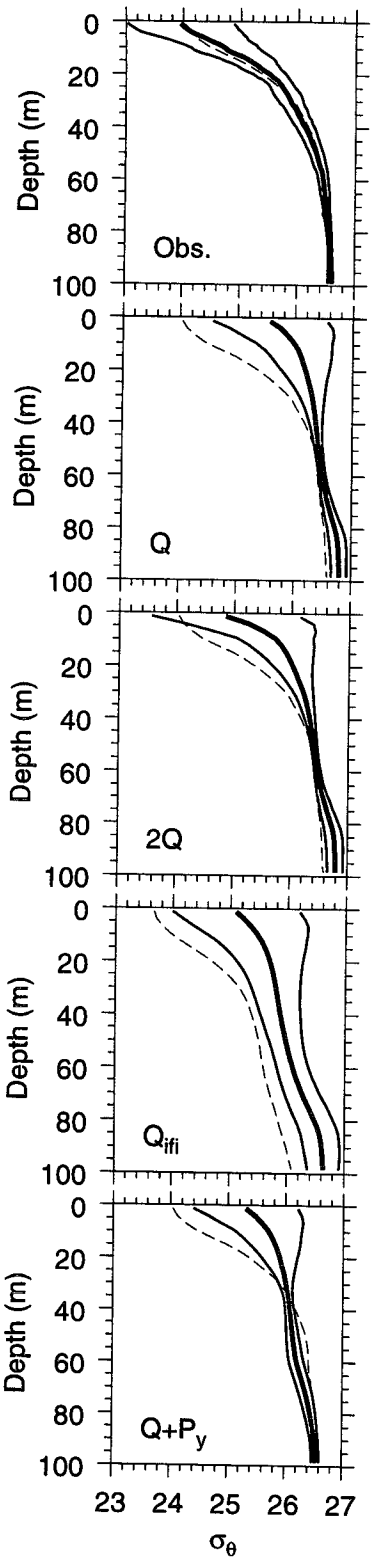

FIG. 18. Mean σ_θ profiles at the 100-m isobath from CTD observations and from experiments Q, $2Q$, Q_{ifi}, and $Q + P_y$. Light solid lines indicate plus and minus one standard deviation and the dashed line shows the initial profile.

disagreement between the model results and field measurements. Smith (1981), in an analysis of the CUE-2 current meter data, found that the onshore flow was stronger than the offshore flow and concluded that the event-scale upwelling process off Oregon is three-dimensional. Allen and Smith (1981), using the same wind and current meter data together with coastal sea level measurements, evaluated the balance of terms in the depth-averaged alongshore momentum equation and found balances consistent with three-dimensional flow. A further indication of three-dimensionality of the observed flow is provided by the model's underpredictions of the means and variances of across-shelf flow. The model u velocities respond only to the local wind, but the observed u field has much greater variability. Three-dimensional effects are likely associated with the alongshore propagation of fluctuations in the form of coastally trapped waves forced by alongshore variations in wind stress. The fluctuations in the observed alongshore currents and coastal sea level during the CUE-2 period show clear evidence of remote forcing (Halliwell and Allen 1984) and these, of course, are not represented in two-dimensional models.

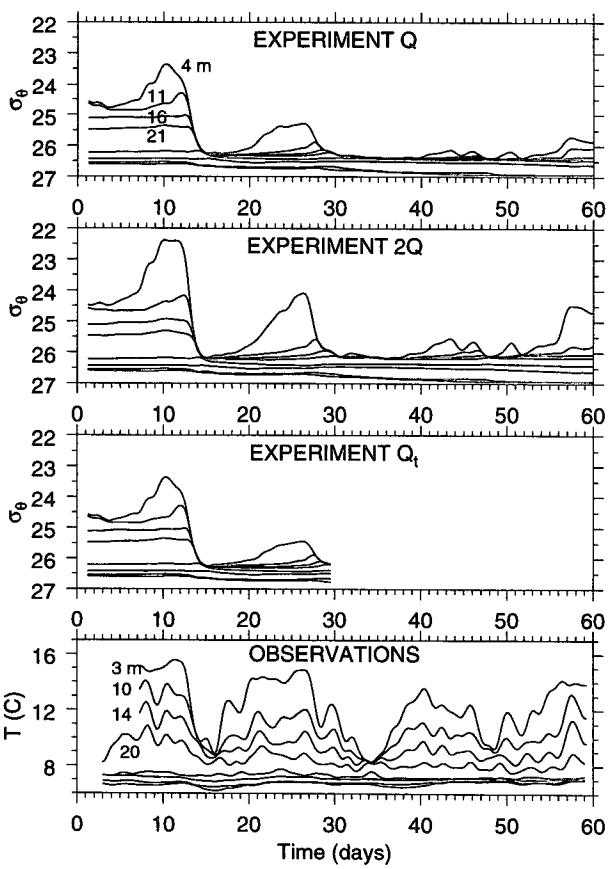

FIG. 19. Time series of low-pass filtered density at the 100-m isobath from experiments Q, $2Q$, and Q_t (depths are 4, 11, 16, 21, 40, 60, 80, and 95 m) and measured temperature from buoy B measurements (depths are 3, 10, 14, 20, 40, 60, 80, and 95 m).

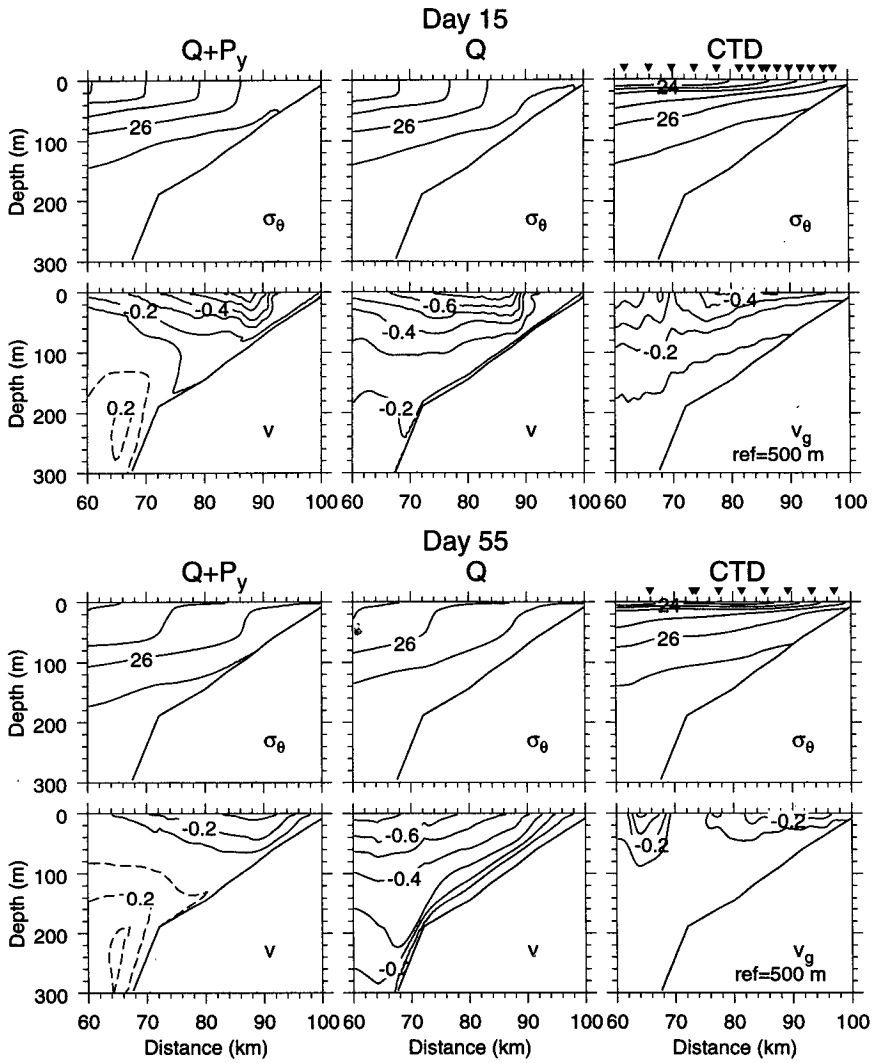

FIG. 20. Comparison of σ_θ and v fields from experiments Q and $Q + P_y$ with CTD measurements on days 15 and 55. Upper: σ_θ from models and CTD measurements; lower: alongshore velocities v from the models, and geostrophic velocity computed from the CTD measured densities above, using a reference level of 500 m and extrapolating by the method of Reid and Mantyla (1976). Contour intervals are $\Delta\sigma_\theta = 0.5$ kg m^{-3} and $\Delta v = 0.1$ m s^{-1}. Triangles indicate locations of CTD profiles.

The success of the model in representing several features of the observed flow field, even with the strong restriction of two-dimensionality, offers promise for the application of direct simulation modeling experiments to studies of the dynamics of the coastal ocean. The importance of forcing function and initial condition specification has been clearly demonstrated. The complex across-shelf circulation patterns found here, with considerable small-scale variability in both space and time, indicate that deterministic modeling of some aspects of the across-shelf circulation is not likely to be possible. Statistical descriptions of the across-shelf velocities will likely be required for proper evaluation of model performance. Further modeling studies and careful model–data comparisons are needed to find the capabilities of shelf circulation models for direct simulations of observed coastal flow fields.

Acknowledgments. This research was supported jointly by the National Science Foundation under Grants OCE-9013263 and OCE-9314317 and by the Office of Naval Research Coastal Sciences Program under Grants N00014-90-J-1050 and N00014-93-1-1301. The authors thank P. Newberger for help with the model implementation and E. Kunze and K. Brink for helpful discussions or comments. We are especially grateful to S. Lentz for a thoughtful review of the manuscript and for providing surface heat flux data.

REFERENCES

Allen, J. S., and R. L. Smith, 1981: On the dynamics of wind-driven shelf currents. *Phil. Trans. Roy. Soc. London* A, **302,** 617–634.

——, P. A. Newberger, and J. Federiuk, 1995: Upwelling circulation on the Oregon continental shelf. Part I: Response to idealized forcing. *J. Phys. Oceanogr.,* **25,** 1843–1866.

Battisti, D. S., and B. M. Hickey, 1984: Application of remote wind-forced coastal trapped wave theory to the Oregon and Washington coasts. *J. Phys. Oceanogr.,* **14,** 887–903.

Blumberg, A. F., and G. L. Mellor, 1987: A description of a three-dimensional coastal ocean circulation model. *Three Dimensional Coastal Ocean Models.* Coastal and Estuarine Science Series, Vol. 4, N. Heaps, Ed., Amer. Geophys. Union, 1–16.

Bryden, H. L., D. Halpern, and R. D. Pillsbury, 1980: Importance of eddy heat flux in a heat budget for Oregon coastal waters. *J. Geophys. Res.,* **85,** (C11), 6649–6653.

Chen, D., and D.-P. Wang, 1990: Simulating the time-variable coastal upwelling during CODE-2. *J. Mar. Res.,* **48,** 335–358.

Denbo, D. W., K. Polzin, J. S. Allen, A. Huyer, and R. L. Smith, 1984: Current meter observations over the continental shelf off Oregon and California February 1981–January 1984. Oregon State University Data Report 112, Ref. 84–12, 372 pp.

Dever, E. P., and S. J. Lentz, 1994: Heat and salt balances over the northern California shelf in winter and spring. *J. Geophys. Res.,* **99,** 16 001–16 017.

Halliwell, G. R., and J. S. Allen, 1984: Large-scale sea level response to atmospheric forcing along the west coast of North America, summer 1973. *J. Phys. Oceanogr.,* **14,** 864–886.

Halpern, D., 1976a: Measurements of near-surface wind stress over an upwelling region near the Oregon coast. *J. Phys. Oceanogr.,* **6,** 108–112.

——, 1976b: Structure of a coastal upwelling event observed off Oregon during July 1973. *Deep-Sea Res.,* **23,** 495–508.

——, J. R. Holbrook, and R. M. Reynolds, 1974: A compilation of wind, current and temperature measurements: Oregon, July and August 1973. CUEA Tech. Rep. 6 Ref. M74-73, Department of Oceanography, University of Washington, 190 pp.

Hamilton, P., and R. Rattray, 1978: A numerical model of the depth-dependent wind driven upwelling circulation on a continental shelf. *J. Phys. Oceanogr.,* **8,** 437–457.

Hickey, B. M., 1984: The fluctuating longshore pressure gradient on the Pacific Northwest shelf: A dynamical analysis. *J. Phys. Oceanogr.,* **14,** 276–293.

——, and P. Hamilton, 1980: A spin-up model as a diagnostic tool for interpretation of current and density measurements on the continental shelf of the Pacific Northwest. *J. Phys. Oceanogr.,* **10,** 12–24.

Huyer, A., 1976: A comparison of upwelling events in two locations: Oregon and Northwest Africa. *J. Mar. Res.,* **34** (4), 531–546.

——, 1977: Seasonal variation in temperature, salinity and density over the continental shelf off Oregon. *Limnol. Oceanogr.,* **22,** 442–453.

——, 1983: Coastal upwelling in the California current system. *Progress in Oceanography,* Vol. 12, Pergamon, 259–284.

——, and W. E. Gilbert, 1974: Coastal upwelling experiment hydrographic data report, June–August 1973. College of Oceanography, Oregon State University Data Report 59, Ref 74-8, 102 pp.

Jerlov, N. G., 1976: *Marine Optics.* Elsevier, 231 pp.

Kundu, P. K., J. S. Allen, and R. Smith, 1975: Modal decomposition of the velocity field near the Oregon coast. *J. Phys. Oceanogr.,* **5,** 683–704.

Large, W. G., and S. Pond, 1981: Open ocean momentum flux measurements in moderate to strong winds. *J. Phys. Oceanogr.,* **11,** 324–336.

Lentz, S. J., 1992: The surface boundary layer in coastal upwelling regions. *J. Phys. Oceanogr.,* **22,** 1517–1539.

Martin, P. J., 1985: Simulation of the mixed layer at OWS November and Papa with several models. *J. Geophys. Res.,* **90,** 903–916.

Mellor, G. L., 1986: Numerical simulation and analysis of the mean coastal circulation off California. *Contin. Shelf Res.,* **6,** 689–713.

Pillsbury, R. D., J. S. Bottero, R. E. Still, and W. E. Gilbert, 1974: A compilation of observations from moored current meters. Volume VII: Oregon continental shelf, July–August 1973. CUEA Data Report 21, Reference 74-7, 87 pp.

Pittock, H. L., W. E. Gilbert, A. Huyer, and R. L. Smith, 1982: Observations of sea level, wind and atmospheric pressure at Newport, Oregon 1967–1980. College of Oceanography, Oregon State University, Data Report 98, Ref. 82-12, 158 pp.

Reed, R. K., and D. Halpern, 1974: Radiation measurements off the Oregon coast. July/August 1973. CUEA Data Report 3, PMEL/NOAA Ref. M74-18. [Available from Department of Oceanography, University of Washington, Seattle, WA 98195.]

Reid, J. B., Jr., and A. W. Mantyla, 1976: The effect of geostrophic flow upon coastal sea elevations in the northern North Pacific Ocean. *J. Geophys. Res.,* **81,** 3100–3110.

Rudnick, D. L., and R. E. Davis, 1988: Mass and heat budgets on the Northern California continental shelf. *J. Geophys. Res.,* **93** (C11), 14 013–14 024.

Send, U., 1989: The origin of eddy heat fluxes in the Northern California upwelling regime. *J. Geophys. Res.,* **94,** 871–876.

Smith, R. L., 1981: A comparison of the structure and variability of the flow field in three coastal upwelling regions: Oregon, Northwest Africa, and Peru Coastal Upwelling. *Coastal and Estuarine Sciences,* **1,** 107–118.

UNESCO, 1983: Algorithms for computation of fundamental properties of seawater. UNESCO Technical Paper, No. 44, 53 pp.

Werner, F. E., and B. M. Hickey, 1983: The role of a longshore pressure gradient in Northwest coastal dynamics. *J. Phys. Oceanogr.,* **13,** 395–410.

Zamudio, L., and M. López, 1994: On the effect of the alongshore pressure gradient on numerical simulations over the northern California continental shelf. *J. Geophys. Res.,* **99,** 16 117–16 129.